



ATLAS Note

GROUP-2017-XX

26th February 2021



1

2 WZ + Heavy Flavor Production in pp collisions 3 at $\sqrt{s} = 13$ TeV

4

The ATLAS Collaboration

5

A measurement of WZ produced with an associated heavy flavor jet is performed using 140
6 fb^{-1} of proton-proton collision data at $\sqrt{s} = 13$ TeV from the ATLAS experiment at the
7 LHC. The measurement is performed in the fully leptonic decay mode, $\text{WZ} \rightarrow \ell\bar{\nu}\ell\bar{\nu}$. The
8 cross-section of $\text{WZ} + b\text{-jets}$ is measured to be $X \pm X \pm X$, while the cross-section of $\text{WZ} +$
9 charm is measured as X , with a correlation of X between the two processes.

10

© 2021 CERN for the benefit of the ATLAS Collaboration.

Reproduction of this article or parts of it is allowed as specified in the CC-BY-4.0 license.

11 Contents

12	1 Changes and outstanding items	3
13	1.1 Changelog	3
14	1.1.1 Changes relative to v4	3
15	1.1.2 Changes relative to v3	3
16	1.1.3 Changes relative to v2	4
17	1.1.4 Changes relative to v1	4
18	1.2 Outstanding Items	4
19	2 Executive Summary	5
20	3 Data and Monte Carlo Samples	5
21	3.1 Data Samples	6
22	3.2 Monte Carlo Samples	6
23	4 Object Reconstruction	8
24	4.1 Trigger	8
25	4.2 Light leptons	9
26	4.3 Jets	10
27	4.4 B-tagged Jets	10
28	4.5 Missing transverse energy	11
29	5 Event Selection and Signal Region Definitions	11
30	5.1 Event Preselection	11
31	5.2 Fit Regions	14
32	5.3 Non-Prompt Lepton Estimation	29
33	5.3.1 $t\bar{t}$ Validation	29
34	5.3.2 Z+jets Validation	33
35	6 tZ Interference Studies and Separation Multivariate Analysis	37
36	6.1 Top Mass Reconstruction	38
37	6.2 tZ BDT	38
38	7 Systematic Uncertainties	42
39	8 Results	48
40	8.1 1-jet Fit Results	49
41	8.2 2-jet Fit Results	57
42	9 Conclusion	64
43	Appendices	66

44 1 Changes and outstanding items**45 1.1 Changelog**

46 This is version 5

47 1.1.1 Changes relative to v4

- 48 • Fixed various typos, clarified wording
- 49 • Expanded info about JER uncertainties, theory uncertainties
- 50 • removed a table on lepton selection, included information in the text instead
- 51 • Plotted lepton Pt Z and W for Zjet CR, rather than lep 1 and 2
- 52 • fixed binning in kinematic plots
- 53 • Included prefit and postfit yield tables
- 54 • added signal modelling systematics

55 1.1.2 Changes relative to v3

- 56 • Merged introduction into executive summary, including unblinding details and list of
- 57 SRs/CRs used
- 58 • listed ptag used (p4133), and release (AB 21.2.127)
- 59 • Included table reftab:xsecUnc listing x-sec uncertainties used
- 60 • Removed selection criteria listed in table ?? (QMisID, AmbiguityType) that were removed
- 61 from the analysis
- 62 • specified variable used to make truth jet flavor determination (HadronConeExclTruthLa-
- 63 belID)
- 64 • fixed bug in MtLepMet calculation, updated selection/fits to account for this
- 65 • Included plots of MtLepMet and PtZ, swapped lep 1 and 2 p_T plots for lep W and lep Z
- 66 plots
- 67 • updated tZ BDT training to reduce overfitting, updated plots to include error bars, feature
- 68 importance
- 69 • updated table 7 to clarify selection, fix the tZ_BDT cut used
- 70 • replace a few broken ntuples which included large weight events

- 71 • include DL1r distribution for Z+jets and $t\bar{t}$ VRs
 72 • Expanded section on fakes, included information on derived scale factors from VRs.
 73 • Changed the kinematic plots to include $p_T(Z)$ and $m_T(W)$, list lepton p_T based on W and
 74 Z candidates.

75 **1.1.3 Changes relative to v2**

- 76 • Added alternate VBS samples to include missing b-jet diagrams
 77 • Included a section on tZ interference effects, ??.
 78 • Updated to reflect changes for 2018, including the move to PFlow jets, DL1r, updated
 79 trigger, and updated AnalysisBase version (now 21.2.127)
 80 • Revised fit regions, using separate 1-jet and 2-jet fits, with all 2-j regions included
 81 • updated plots for tZ BDT, added details about the model
 82 • Included truth jet information

83 **1.1.4 Changes relative to v1**

- 84 • Added GRL list
 85 • Fixed latex issue in line 92, typo in line 172
 86 • Added tables 5 and ??, summarizing the event and object selection
 87 • Added table 2, which includes the DSID of samples used
 88 • Included reference to WZ inclusive paper in introduction

89 **1.2 Outstanding Items**

- 90 • Complete interference studies, apply any interference effects observed as a systematic
 91 • Update results section with additional studies, possibly including:
 92 – Truth jet migration studies
 93 – Simultaneous fit over 1j and 2j
 94 – Impact of allowing tZ to float
 95 • Unblind, update plots and fits to include data
 96 • Add cross-section, significance once unblinded

97 2 Executive Summary

98 The production of WZ in association with a heavy flavor jet represents an important background
 99 for many major analyses. This includes any process with leptons and b-jets in the final state,
 100 such as $t\bar{t}H$, $t\bar{t}W$, and $t\bar{t}Z$. While precise measurements have been made of WZ production
 101 [1], $WZ +$ heavy flavor remains poorly understood. This is largely because the QCD processes
 102 involved in the production of the b-jet make it difficult to simulate accurately. This introduces a
 103 large uncertainty for analyses that include this process as a background.

104 Motivated by its relevance to the $t\bar{t}H$ multilepton analysis, we perform a study of the fully
 105 leptonic decay mode of this channel; that is, events where both the W and Z decay leptonically.
 106 Because WZ has no associated jets at leading order, while the major backgrounds for this channel
 107 tend to have high jet multiplicity, events with more than two jets are rejected. This gives a final
 108 state signature of three leptons and one or two jets.

109 Events that meet this selection criteria are sorted into pseudo-continuous b-tagging regions based
 110 on the DL1r b-tag score of their associated jets. This is done to separate $WZ +$ b-jet events from
 111 $WZ +$ charm and $WZ +$ light jets. These regions are fit to data in order make a more accurate
 112 estimate of the contribution of $WZ +$ heavy-flavor, where heavy-flavor jets include b-jets and
 113 charm jets. The full Run-2 dataset collected by the ATLAS detector, representing 139 fb^{-1} of
 114 data from pp collisions at $\sqrt{s} = 13 \text{ TeV}$, is used for this study.

115 All backgrounds are accounted for using Monte Carlo, with the simulation of non-prompt lepton
 116 backgrounds - $Z+jets$ and $t\bar{t}$ - validated using non-prompt Validation Regions.

117 Section 3 details the data and Monte Carlo (MC) samples used in the analysis. The reconstruction
 118 of various physics objects is described in section 4. Section 5 describes the event selection applied
 119 to these samples, along the definitions of the various regions used in the fit. The multivariate
 120 analysis techniques used to separate the tZ background from $WZ +$ heavy flavor are described in
 121 section 6. Section 7 describes the various sources of systematic uncertainties considered in the
 122 fit. Finally, the results of the analysis are summarized in section 8, followed by a brief conclusion
 123 in section 9.

124 The current state of thee analysis shows blinded results for thee full Run 2 dataset. Regions
 125 containing $>5\%$ $WZ+b$ events are blinded, and results are from Asimov, MC only fits. In
 126 addition to adding some additional information to this note, remaining tasks include performing
 127 WZ/tZ interference studies, finalizing the presentation of results, and unblinding.

128 3 Data and Monte Carlo Samples

129 Both data and Monte Carlo samples used in this analysis were prepared in the `xAOD` format,
 130 which was used to produce a `DxAOD` sample in the `HIGG8D1` derivation framework. The `HIGG8D1`
 131 framework is designed for the $t\bar{t}H$ multi-lepton analysis, which targets events with multiple
 132 leptons as well as tau hadrons. This framework skims the dataset to remove unneeded variables

133 as well as entire events. Events are removed from the derivations that do not meet the following
 134 selection:

- 135 • at least two light leptons within a range $|\eta| < 2.6$, with leading lepton $p_T > 15$ GeV and
 136 subleading lepton $p_T > 5$ GeV
- 137 • at least one light lepton with $p_T > 15$ GeV within a range $|\eta| < 2.6$, and at least two hadronic
 138 taus with $p_T > 15$ GeV.

139 Samples were then generated from these HIGG8D1 derivations with p-tag of p4134 using Ana-
 140 lysisBase version 21.2.127 modified to include custom variables..

141 **3.1 Data Samples**

142 The study uses a sample of proton-proton collision data collected by the ATLAS detector from
 143 2015 through 2018 at an energy of $\sqrt{s} = 13$ TeV, which represents an integrated luminosity of
 144 139 fb^{-1} . This data set was collected with a bunch crossing rate of 25 ns. All data used in this
 145 analysis was verified by data quality checks, having been included in the following Good Run
 146 Lists:

- 147 • data15_13TeV.periodAllYear_DetStatus-v79-repro20-02_DQDefects-00-02-02
 148 _PHYS_StandardGRL_All_Good_25ns.xml
- 149 • data16_13TeV.periodAllYear_DetStatus-v88-pro20-21_DQDefects-00-02-04
 150 _PHYS_StandardGRL_All_Good_25ns.xml
- 151 • data17_13TeV.periodAllYear_DetStatus-v97-pro21-13_Unknown_PHYS_StandardGRL
 152 _All_Good_25ns_Triggerno17e33prim.xml
- 153 • data18_13TeV.periodAllYear_DetStatus-v102-pro22-04_Unknown_PHYS_StandardGRL
 154 _All_Good_25ns_Triggerno17e33prim.xml

155 Runs included from the AllYear period containers are included.

156 **3.2 Monte Carlo Samples**

157 Several different generators were used to produce Monte Carlo simulations of the signal and
 158 background processes. For all samples, the response of the ATLAS detector is simulated using
 159 Geant4. The WZ signal samples are simulated using Sherpa 2.2.2 [2]. Specific information
 160 about the Monte Carlo samples being used can be found in table 1. A list of the specific samples
 161 used by data set ID is shown in table 2.

Table 1: The configurations used for event generation of signal and background processes, including the event generator, matrix element (ME) order, parton shower algorithm, and parton distribution function (PDF).

Process	Event generator	ME order	Parton Shower	PDF
WZ, VV	SHERPA 2.2.2	MEPS NLO	SHERPA	CT10
tZ	MG5_AMC	LO	PYTHIA 6	CTEQ6L1
t̄W	MG5_AMC (SHERPA 2.1.1)	NLO (LO multileg)	PYTHIA 8 (SHERPA)	NNPDF 3.0 NLO (NNPDF 3.0 NLO)
t̄t(Z/γ* → ll)	MG5_AMC	NLO	PYTHIA 8	NNPDF 3.0 NLO
t̄tH	MG5_AMC (MG5_AMC)	NLO (NLO)	PYTHIA 8 (HERWIG++)	NNPDF 3.0 NLO [Ball:2014uwa] (CT10 [ct10])
tHqb	MG5_AMC	LO	PYTHIA 8	CT10
tHW	MG5_AMC (SHERPA 2.1.1)	NLO (LO multileg)	HERWIG++ (SHERPA)	CT10 (NNPDF 3.0 NLO)
tWZ	MG5_AMC	NLO	PYTHIA 8	NNPDF 2.3 LO
t̄t, t̄t̄t̄	MG5_AMC	LO	PYTHIA 8	NNPDF 2.3 LO
t̄tW+W-	MG5_AMC	LO	PYTHIA 8	NNPDF 2.3 LO
t̄t	Powheg-BOX v2 [powheg tt]	NLO	PYTHIA 8	NNPDF 3.0 NLO
t̄tγ	MG5_AMC	LO	PYTHIA 8	NNPDF 2.3 LO
s-, t-channel, Wt single top	Powheg-BOX v1 [powheg stp]	NLO	PYTHIA 6	CT10
qqVV, VVV Z → l+l-	SHERPA 2.2.1	MEPS NLO	SHERPA	NNPDF 3.0 NLO

Sample	DSID
WZ	364253, 364739-42
VV	364250, 364254, 364255, 363355-60, 364890
t̄W	410155
t̄Z	410156, 410157, 410218-20
low mass t̄Z	410276-8
Rare Top	410397, 410398, 410399
single Top	410658-9, 410644-5
three Top	304014
four Top	410080
t̄WW	410081
Z + jets	364100-41
low mass Z + jets	364198-215
W + jets	364156-97
Vγ	364500-35
tZ	410560
tW	410013-4
WtZ	410408
VVV	364242-9
VH	342284-5
WtH	341998
t̄tγ	410389
t̄t	410470
t̄tH	345873-5, 346343-5

Table 2: List of Monte Carlo samples by data set ID used in the analysis.

162 4 Object Reconstruction

163 All regions defined in this analysis share a common lepton, jet, and overall event preselection.
 164 The selection applied to each physics object is detailed here; the event preselection, and the
 165 selection used to define the various fit regions, is described in section 5.

166 4.1 Trigger

167 Events are required to be selected by dilepton triggers, as summarized in table 3.

Dilepton triggers (2015)	
$\mu\mu$ (asymm.)	HLT_mu18_mu8noL1
ee (symm.)	HLT_2e12_lhloose_L12EM10VH
$e\mu, \mu e$ (\sim symm.)	HLT_e17_lhloose_mu14
Dilepton triggers (2016)	
$\mu\mu$ (asymm.)	HLT_mu22_mu8noL1
ee (symm.)	HLT_2e17_lhvloose_nod0
$e\mu, \mu e$ (\sim symm.)	HLT_e17_lhloose_nod0_mu14
Dilepton triggers (2017)	
$\mu\mu$ (asymm.)	HLT_mu22_mu8noL1
ee (symm.)	HLT_2e24_lhvloose_nod0
$e\mu, \mu e$ (\sim symm.)	HLT_e17_lhloose_nod0_mu14
Dilepton triggers (2018)	
$\mu\mu$ (asymm.)	HLT_mu22_mu8noL1
ee (symm.)	HLT_2e24_lhvloose_nod0
$e\mu, \mu e$ (\sim symm.)	HLT_e17_lhloose_nod0_mu14

Table 3: List of lowest p_T -threshold, un-prescaled dilepton triggers used for 2015–2018 data taking.

168 4.2 Light leptons

169 Electron candidates are reconstructed from energy clusters in the electromagnetic calorimeter
 170 that are associated with charged particle tracks reconstructed in the inner detector [3]. Electron
 171 candidates are required to have $p_T > 10$ GeV and $|\eta_{\text{cluster}}| < 2.47$. Muon candidates are
 172 reconstructed by combining inner detector tracks with track segments or full tracks in the muon
 173 spectrometer [4]. Muon candidates are required to have $p_T > 10$ GeV and $|\eta| < 2.5$. Candidates
 174 in the transition region between different electromagnetic calorimeter components, $1.37 <$
 175 $|\eta_{\text{cluster}}| < 1.52$, are rejected. A multivariate likelihood discriminant combining shower shape
 176 and track information is used to distinguish real electrons from hadronic showers (fake electrons).
 177 To further reduce the non-prompt electron contribution, the track is required to be consistent
 178 with originating from the primary vertex; requirements are imposed on the transverse impact
 179 parameter significance ($|d_0|/\sigma_{d_0} < 5$) and the longitudinal impact parameter ($|\Delta z_0 \sin \theta_\ell| < 0.5$
 180 mm).

181 Muon candidates are reconstructed by combining inner detector tracks with track segments or
 182 full tracks in the muon spectrometer [4]. Muon candidates are required to have $p_T > 10$ GeV
 183 and $|\eta| < 2.5$. The longitudinal impact parameter is the same for both electrons and muons, while
 184 muons are required to pass a slightly tighter transverse impact parameter, $|d_0|/\sigma_{d_0} < 3$.

185 All leptons are required to be isolated, as defined through the standard `isolationFixedCutLoose`
 186 working point supported by combined performance groups. Leptons are additionally required to
 187 pass a non-prompt BDT selection described in detail in [5]. Optimized working points and scale
 188 factors for this BDT are taken from that analysis.

189 4.3 Jets

190 Jets are reconstructed from calibrated topological clusters built from energy deposits in the
 191 calorimeters [6], using the anti- k_t algorithm with a radius parameter $R = 0.4$. Jets with energy
 192 contributions likely arising from noise or detector effects are removed from consideration [7],
 193 and only jets satisfying $p_T > 25$ GeV and $|\eta| < 2.5$ are used in this analysis. For jets with
 194 $p_T < 60$ GeV and $|\eta| < 2.4$, a jet-track association algorithm is used to confirm that the jet
 195 originates from the selected primary vertex, in order to reject jets arising from pileup collisions
 196 [8].

197 4.4 B-tagged Jets

198 In order to make a measurement of $WZ +$ heavy flavor it is necessary to distinguish these events
 199 from $WZ +$ light jets. For this purpose, the DL1r b-tagging algorithm is used to distinguish
 200 heavy flavor jets from lighter ones. The DL1r algorithm uses jet kinematics, particularly jet
 201 vertex information, as input for a neural network which assigns each jet a score designed to
 202 reflect how likely that jet is to have originated from a b-quark.

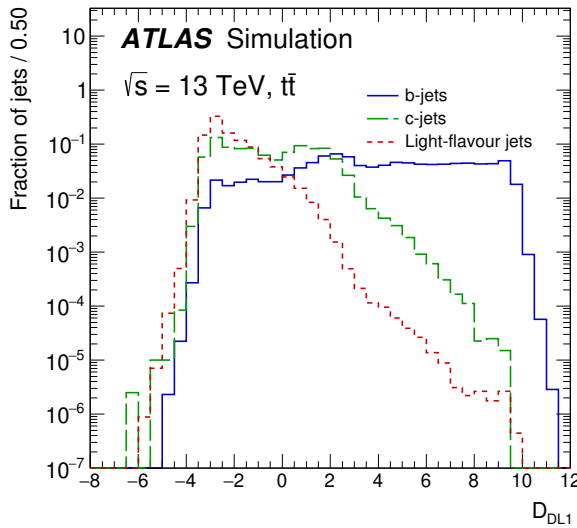


Figure 1: Output distribution of the DL1r algorithm for b-jets, charm jets, and light jets

203 From the output of the BDT, working points (WPs) are developed based on the efficiency of truth
 204 b-jets at particular values of the DL1r algorithm. The working points used in this analysis are
 205 summarized in table 4.

WP	none	loose	medium	tight	tightest
b eff.	-	85%	77%	70%	60%

Table 4: B-tagging Working Points by tightness and b-jet efficiency

206 A tighter WP will accept fewer b-jets, but reject a higher fraction of charm and light jets.
 207 Generally, analyses that include b-jets will use a fixed working point, for example, requiring that
 208 a jet pass the 70% threshold. By instead treating these working point as bins, e.g. events with
 209 jets that fall between the 85% and 77% WPs fall into one bin, while events with jets passing the
 210 60% WP fall into another, and looking at the full psuedo-continuous DL1r spectrum of the jets,
 211 additional information can be gained. The psuedo-continuous b-tag spectrum is used in this case
 212 to separate out WZ + b, WZ + charm, and WZ + light.

213 4.5 Missing transverse energy

214 Missing transverse momentum (E_T^{miss}) is used as part of the event selection. The missing
 215 transverse momentum vector is defined as the inverse of the sum of the transverse momenta of
 216 all reconstructed physics objects as well as remaining unclustered energy, the latter of which is
 217 estimated from low- p_T tracks associated with the primary vertex but not assigned to a hard object,
 218 with object definitions taken from [9]. Light leptons considered in the E_T^{miss} reconstruction are
 219 required to have $p_T > 10$ GeV, while jets are required to have $p_T > 20$ GeV.

220 5 Event Selection and Signal Region Definitions

221 Event are required to pass a preselection described in section 5.1 and summarized in table 5.
 222 Those that pass this preselection are divided into various fit regions described in section 5.2,
 223 based on the number of jets in the event, and the b-tag score of those jets.

224 5.1 Event Preselection

225 Events are required to include exactly three reconstructed light leptons passing the requirement
 226 described in 4.2, which have a total charge of ± 1 . As the opposite sign lepton is found to be
 227 prompt the vast majority of the time [5], it is required to be loose and isolated, as defined though
 228 the standard `isolationFixedCutLoose` working point supported by combined performance

229 groups. The same sign leptons are required to be very tightly isolated, as per the recommended
 230 `isolationFixedCutTight`.

231 The leptons are ordered in the analysis code as 0, 1, and 2. Lepton 0 is the lepton whose charge
 232 is opposite the other two. Lepton 1 is the lepton closest to the opposite charge lepton, i.e. the
 233 smallest ΔR , leaving lepton 2 as the lepton further from the opposite charge lepton. Lepton 0
 234 is required to have $p_T > 10$ GeV, while the same sign leptons, 1 and 2, are required to have
 235 $p_T > 20$ GeV to reduce the contribution of non-prompt leptons.

236 The invariant mass of at least one pair of opposite sign, same flavor leptons is required to fall
 237 within 10 GeV of the mass of the Z boson, 91.2 GeV. Events where one of the opposite sign pairs
 238 have an invariant mass less than 12 GeV are rejected in order to suppress low mass resonances.

239 An additional requirement is placed on the missing transverse energy, $E_T^{\text{miss}} > 20$ GeV, and the
 240 transverse mass of the W candidate, $m(E_T^{\text{miss}} + l_{\text{other}}) > 30$ GeV, where E_T^{miss} is the missing
 241 transverse energy, and l_{other} is the lepton not included in the Z-candidate.

242 Events are required to have one or two reconstructed jets passing the selection described in
 243 section 4.3. Events with more than two jets are rejected in order to reduce the contribution of
 244 backgrounds such as $t\bar{t}Z$ and $t\bar{t}W$, which tend to have higher jet multiplicity.

Event Selection

- Exactly three leptons with charge ± 1
 - Two tight Iso, tight ID same-charge leptons with $p_T > 20$ GeV
 - One loose Iso, medium ID opposite charge lepton with $p_T > 10$ GeV
 - $m(l^+l^-)$ within 10 GeV of 91.2 GeV
 - Transverse mass of W-candidate, $m_T(E_T^{\text{miss}} + \text{lep}_{\text{other}}) > 30$ GeV
 - Missing transverse energy, $E_T^{\text{miss}} > 20$ GeV
 - One or two jets with $p_T > 25$ GeV
-

Table 5: Summary of the selection applied to events for inclusion in the fit

245 The event yields in the preselection region for both data and Monte Carlo are summarized in
 246 table 5.1, which shows good agreement between data and Monte Carlo, and demonstrates that
 247 this region consists primarily of WZ events. The WZ events are split into WZ + b, WZ + c, and
 248 WZ + l based on the truth flavor of the associated jet in the event. Specifically, this determination
 249 is made based on the `HadronConeExclTruthLabelID` of the jet, as recommended by the b-
 250 tagging working group [BtagWG]. In this ordering b-jet supersedes charm, which supersedes
 251 light. That is, WZ + l events contain no charm and no b jets at truth level, WZ + c contain at
 252 least one truth charm and no b-jets, and WZ + b contains at least one truth b-jet.

Process	Events
WZ + b	167.6 ± 6.5
WZ + c	1080 ± 40
WZ + l	7220 ± 310
Other VV	850 ± 140
t̄tW	16.8 ± 2.3
t̄tZ	115 ± 17
rare Top	2.2 ± 0.1
Single top	0.10 ± 0.45
Three top	0.01 ± 0.01
Four top	0.02 ± 0.01
t̄tWW	0.23 ± 0.05
Z + jets	600 ± 260
V + γ	37 ± 54
tZ	190 ± 70
tW	5.5 ± 1.2
WtZ	25.8 ± 1.1
VVV	26.2 ± 0.9
VH	94 ± 7
t̄t	108.68 ± 8
t̄tH	4.3 ± 0.5
Total	10600 ± 530
Data	10574

Table 6: Event yields in the preselection region at 139.0 fb^{-1}

253 Here Other VV represents diboson processes other than WZ, and consists predominantly of
254 ZZ → ll̄ll events where one of the leptons is not reconstructed.

255 Simulations are further validated by comparing the kinematic distributions of the Monte Carlo
256 with data, which are shown in figure 2. Here, bins with 5% or more WZ+b are blinded.

WZ Fit Region - Inclusive

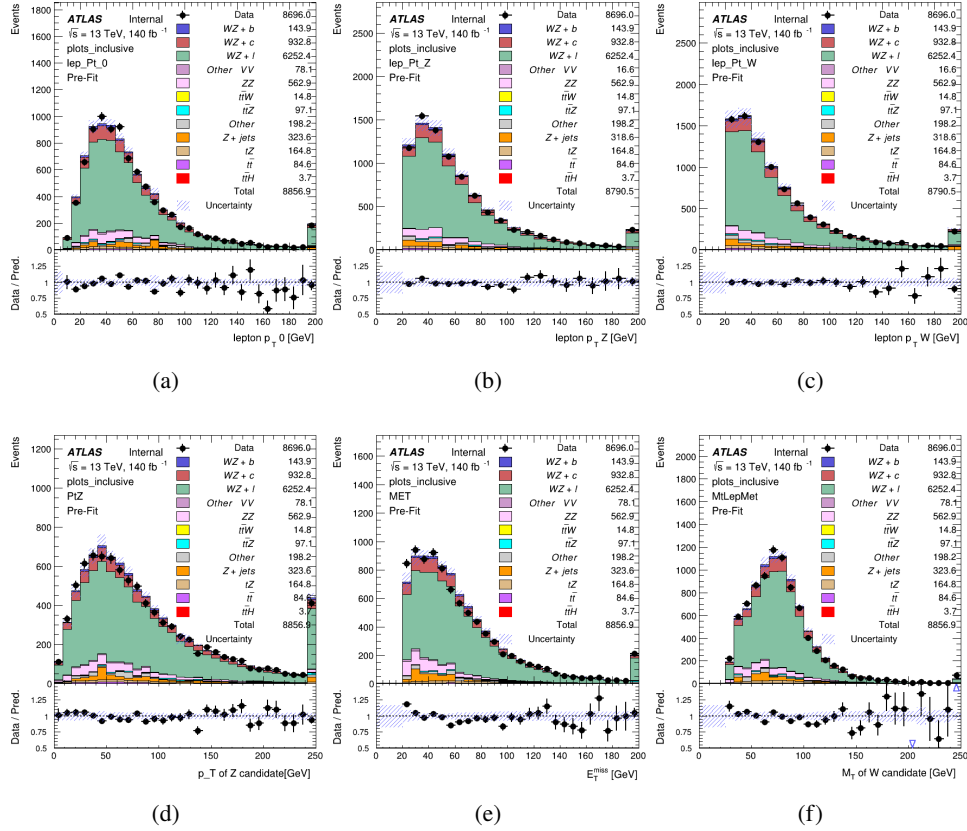


Figure 2: Comparisons between the data and MC distributions in the preselection region for (a) the p_T of the opposite sign lepton, (b) the p_T of the other lepton from the Z candidate, (c) the p_T of the lepton from the W candidate, (d) the p_T of the Z candidate, (e) the E_T^{miss} , and (f) the M_T of the W candidate.

5.2 Fit Regions

Once preselection has been applied, the remaining events are categorized into one of twelve orthogonal regions. The regions used in the fit are summarized in table 7.

Table 7: A list of the regions used in the fit and the selection used for each.

Region	Selection
1j, <85%	$N_{\text{jets}} = 1, n\text{Jets_DL1r_85} = 0$
1j, 85%-77%	$N_{\text{jets}} = 1, n\text{Jets_DL1r_85} = 1, n\text{Jets_DL1r_77}=0$
1j, 77%-70%	$N_{\text{jets}} = 1, n\text{Jets_DL1r_77} = 1, n\text{Jets_DL1r_70}=0$
1j, 70%-60%	$N_{\text{jets}} = 1, n\text{Jets_DL1r_70} = 1, n\text{Jets_DL1r_60}=0$
1j, >60%	$N_{\text{jets}} = 1, n\text{Jets_DL1r_60} = 1, tZ \text{ BDT} > 0.725$
1j tZ CR	$N_{\text{jets}} = 1, n\text{Jets_DL1r_60} = 1, tZ \text{ BDT} < 0.725$
2j, <85%	$N_{\text{jets}} = 2, n\text{Jets_DL1r_85} = 0$
2j, 85%-77%	$N_{\text{jets}} = 2, n\text{Jets_DL1r_85} >= 1, n\text{Jets_DL1r_77}=0$
2j, 77%-70%	$N_{\text{jets}} = 2, n\text{Jets_DL1r_77} >= 1, n\text{Jets_DL1r_70}=0$
2j, 70%-60%	$N_{\text{jets}} = 2, n\text{Jets_DL1r_70} >= 1, n\text{Jets_DL1r_60}=0$
2j, >60%	$N_{\text{jets}} = 2, n\text{Jets_DL1r_60} >= 1, tZ \text{ BDT} > 0.725$
2j tZ CR	$N_{\text{jets}} = 2, n\text{Jets_DL1r_60} >= 1, tZ \text{ BDT} < 0.725$

- 260 The working points discussed in section 4.4 are used to separate events into fit regions based on
 261 the highest working point reached by a jet in each event. Because the background composition
 262 differs significantly based on the number of b-jets, events are further subdivided into 1 jet and 2
 263 jet regions in order to minimize the impact of background uncertainties.
- 264 An additional tZ control region is created based on the BDT described in section 6. The region
 265 with 1-jet passing the 60% working point is split in two - a signal enriched region of events with
 266 a BDT score greater than 0.03, and a tZ control region including events with less than 0.03. This
 267 cutoff is arrived at by performing an Asimov fit with a variety of cutoffs, and selecting the value
 268 that produces the highest significance for the measurement of WZ + b.
- 269 The modeling in each region is validated by comparing data and MC predictions for various
 270 kinematic distributions. These plot are shown in figures 3-16.

WZ Fit Region - 1j Inclusive

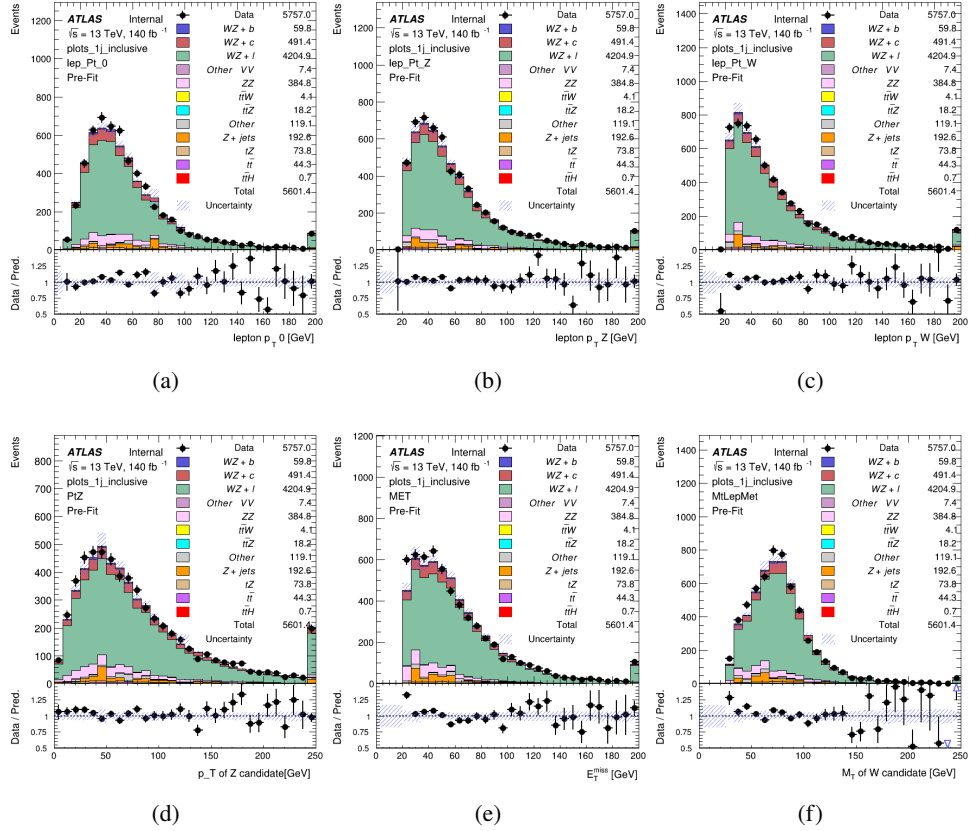


Figure 3: Comparisons between the data and MC distributions in the preselection region for (a) the p_T of the opposite sign lepton, (b) the p_T of the other lepton from the Z candidate, (c) the p_T of the lepton from the W candidate, (d) the p_T of the Z candidate, (e) the E_T^{miss} , and (f) the M_T of the W candidate.

WZ Fit Region - 1j < 85% WP

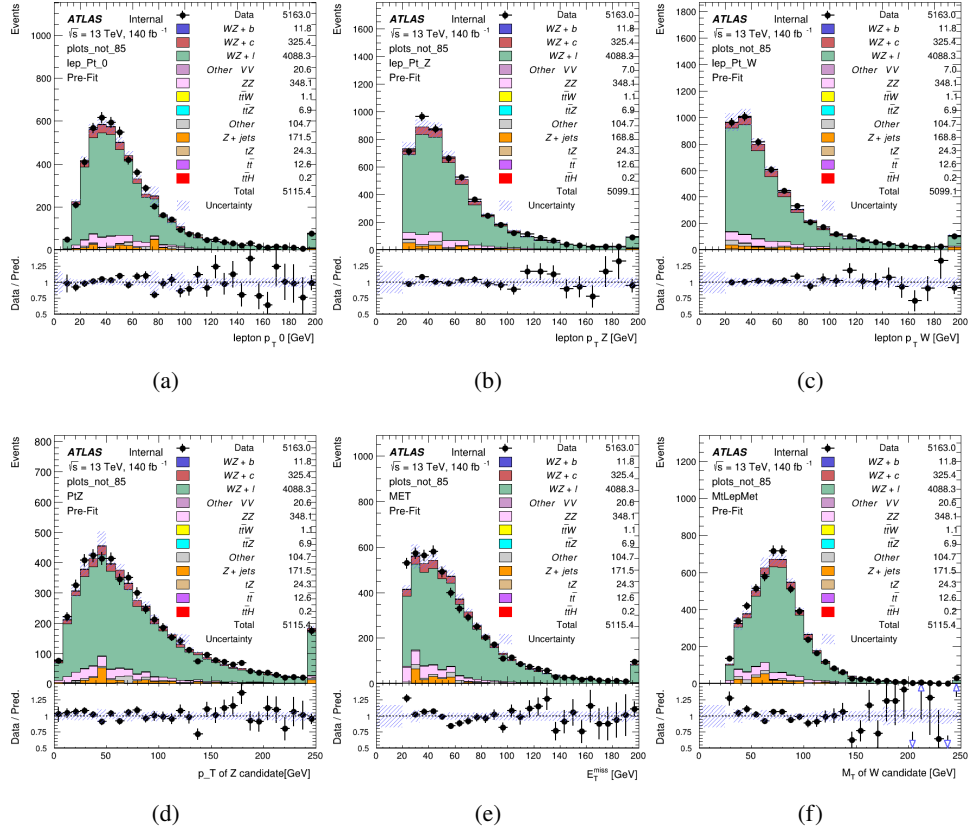


Figure 4: Comparisons between the data and MC distributions in the preselection region for (a) the p_T of the opposite sign lepton, (b) the p_T of the other lepton from the Z candidate, (c) the p_T of the lepton from the W candidate, (d) the p_T of the Z candidate, (e) the E_T^{miss} , and (f) the m_T of the W candidate.

WZ Fit Region - 1j 77-85% WP

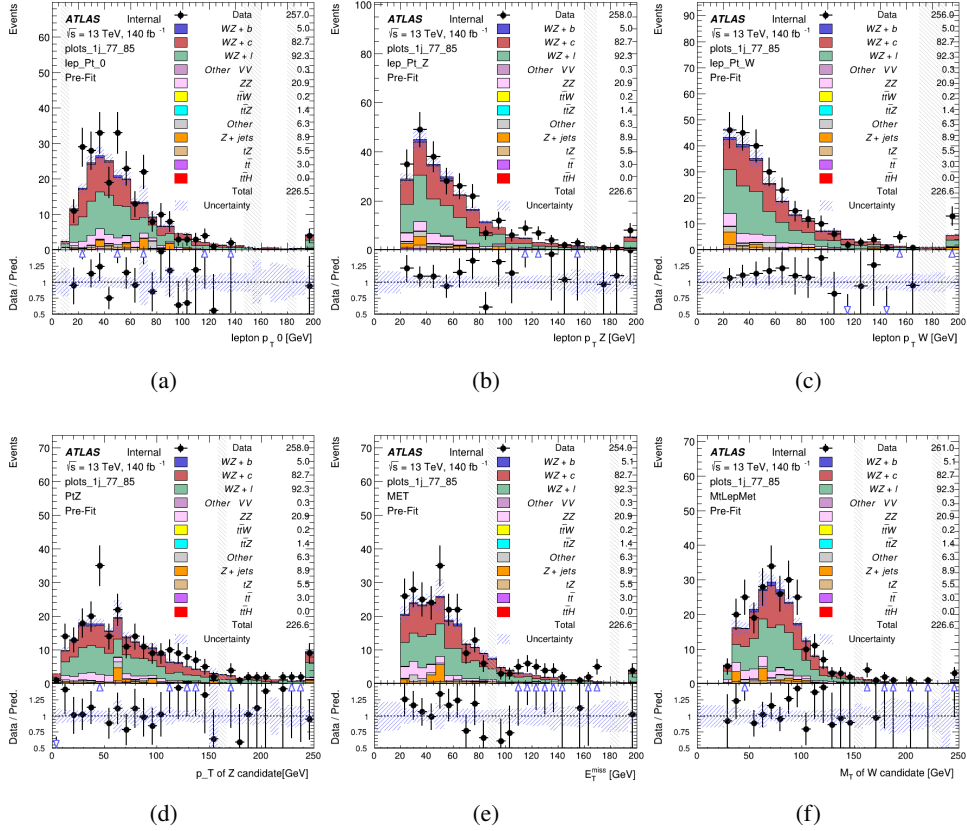


Figure 5: Comparisons between the data and MC distributions in the preselection region for (a) the p_T of the opposite sign lepton, (b) the p_T of the other lepton from the Z candidate, (c) the p_T of the lepton from the W candidate, (d) the p_T of the Z candidate, (e) the E_T^{miss} , and (f) the m_T of the W candidate.

WZ Fit Region - 1j 70-77% WP

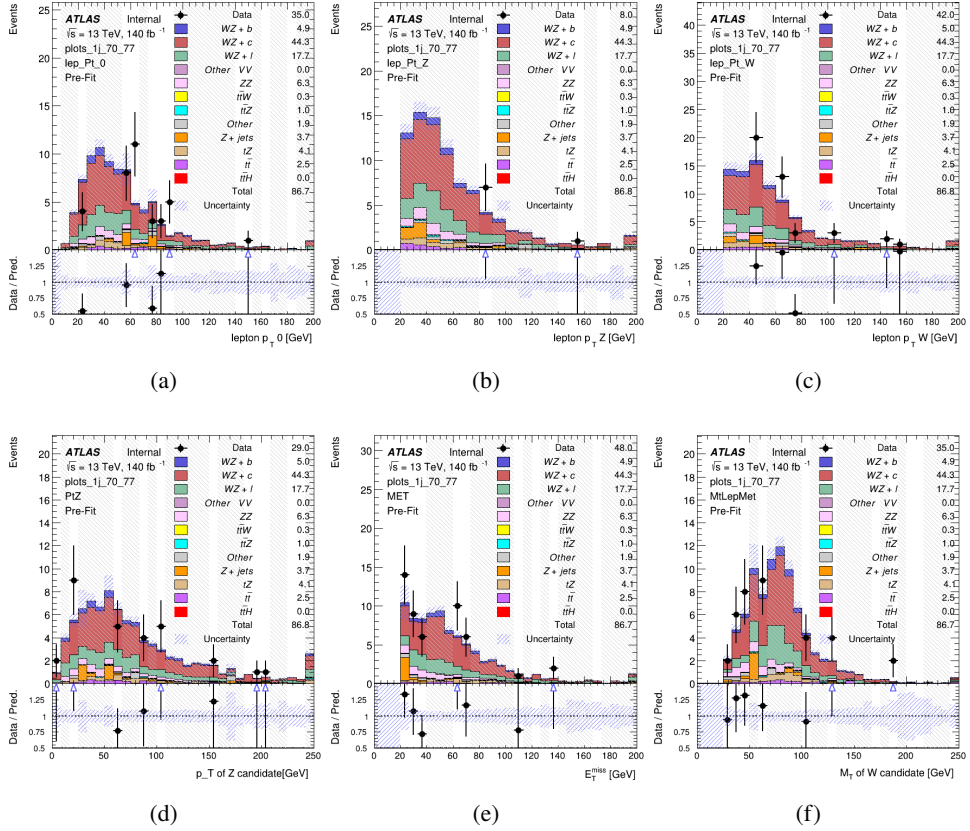


Figure 6: Comparisons between the data and MC distributions in the preselection region for (a) the p_T of the opposite sign lepton, (b) the p_T of the other lepton from the Z candidate, (c) the p_T of the lepton from the W candidate, (d) the p_T of the Z candidate, (e) the E_T^{miss} , and (f) the m_T of the W candidate.

WZ Fit Region - 1j 60-70% WP

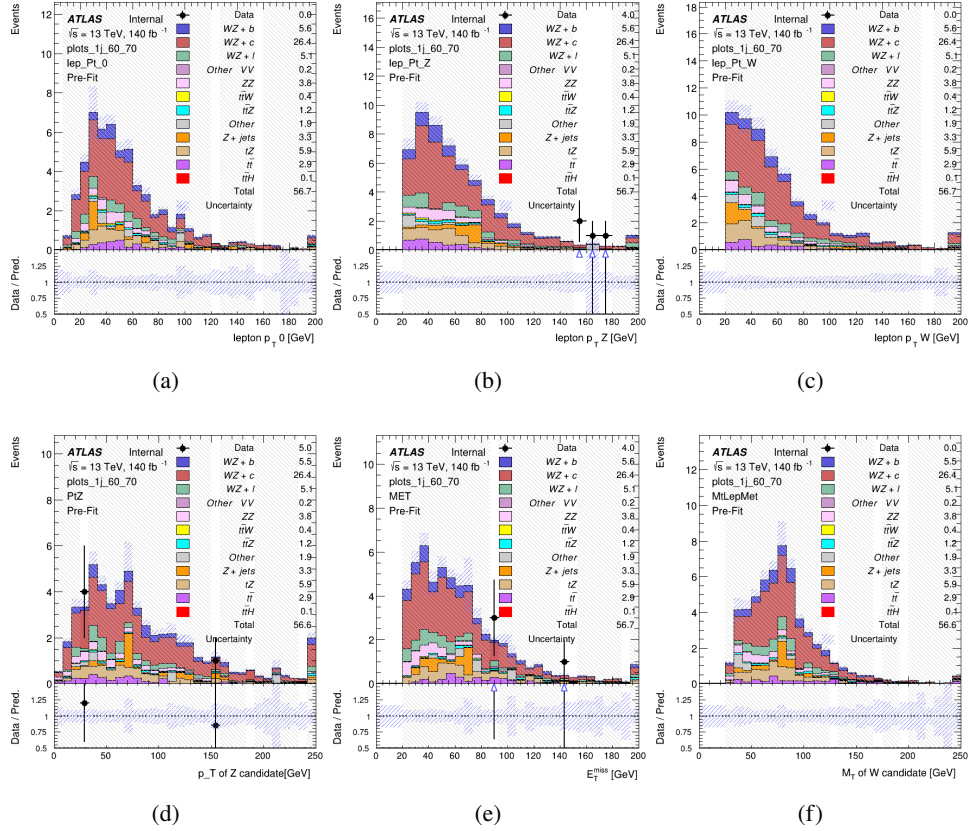


Figure 7: Comparisons between the data and MC distributions in the preselection region for (a) the p_T of the opposite sign lepton, (b) the p_T of the other lepton from the Z candidate, (c) the p_T of the lepton from the W candidate, (d) the p_T of the Z candidate, (e) the E_T^{miss} , and (f) the m_T of the W candidate.

WZ Fit Region - 1j 60% WP

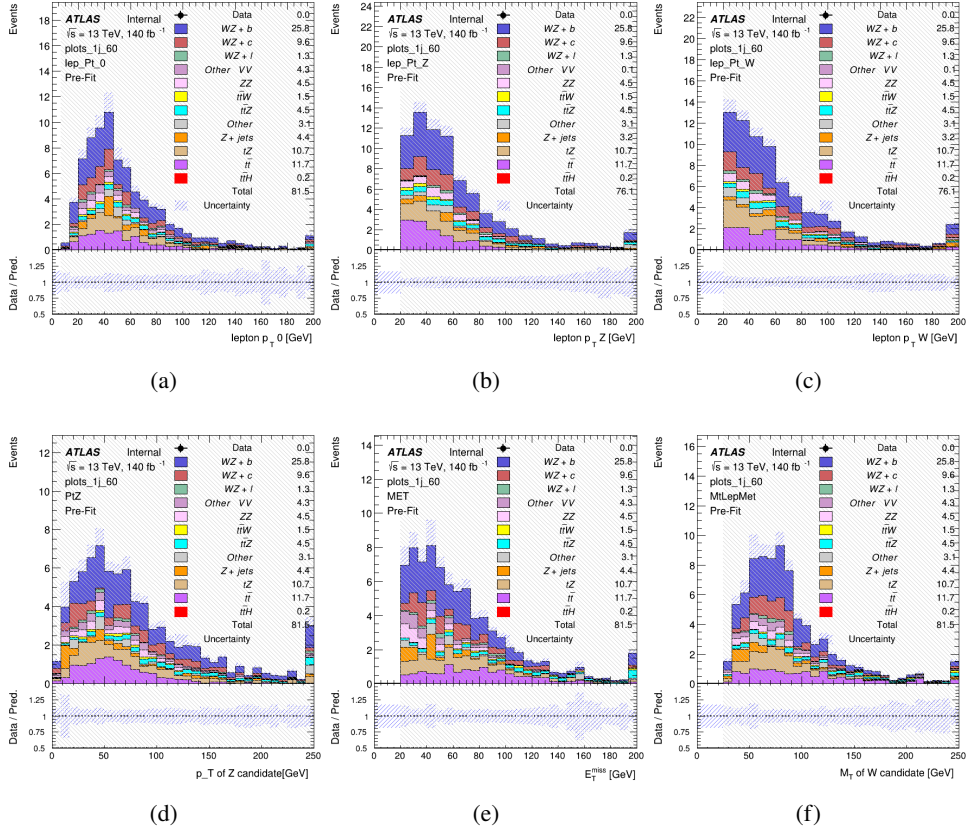


Figure 8: Comparisons between the data and MC distributions in the preselection region for (a) the p_T of the opposite sign lepton, (b) the p_T of the other lepton from the Z candidate, (c) the p_T of the lepton from the W candidate, (d) the p_T of the Z candidate, (e) the E_T^{miss} , and (f) the m_T of the W candidate.

WZ Fit Region - tZ-CR

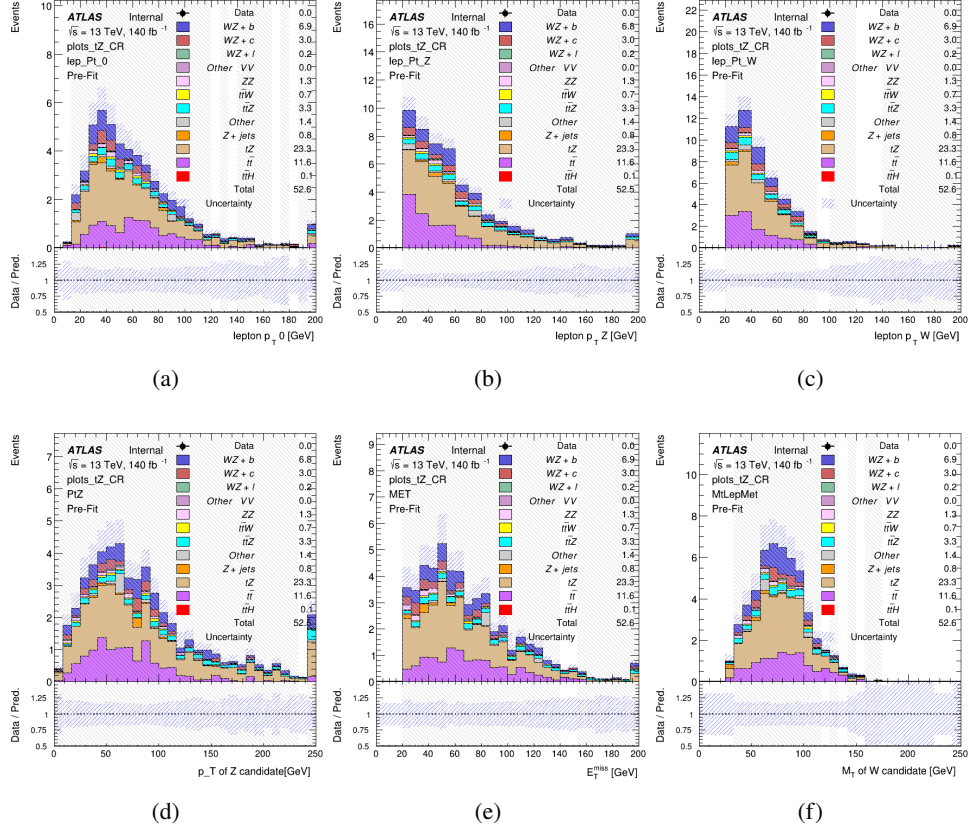


Figure 9: Comparisons between the data and MC distributions in the preselection region for (a) the p_T of the opposite sign lepton, (b) the p_T of the other lepton from the Z candidate, (c) the p_T of the lepton from the W candidate, (d) the p_T of the Z candidate, (e) the E_T^{miss} , and (f) the m_T of the W candidate.

WZ Fit Region - 2j Inclusive

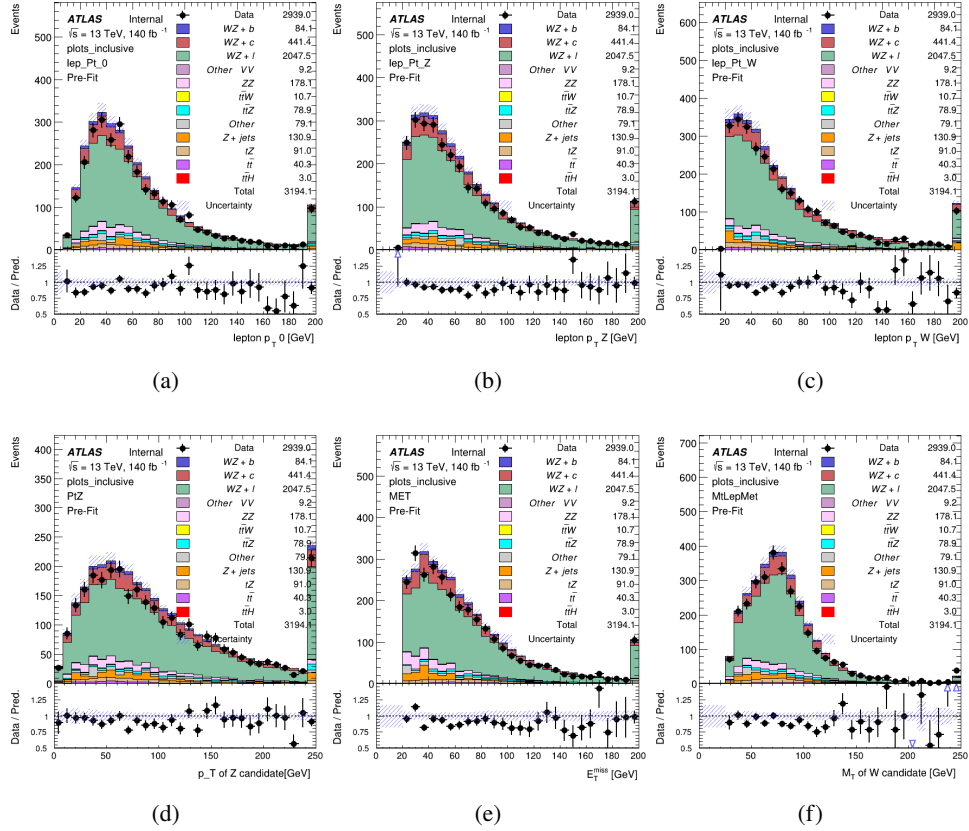


Figure 10: Comparisons between the data and MC distributions in the preselection region for (a) the p_T of the opposite sign lepton, (b) the p_T of the other lepton from the Z candidate, (c) the p_T of the lepton from the W candidate, (d) the p_T of the Z candidate, (e) the E_T^{miss} , and (f) the M_T of the W candidate.

WZ Fit Region - 2j < 85% WP

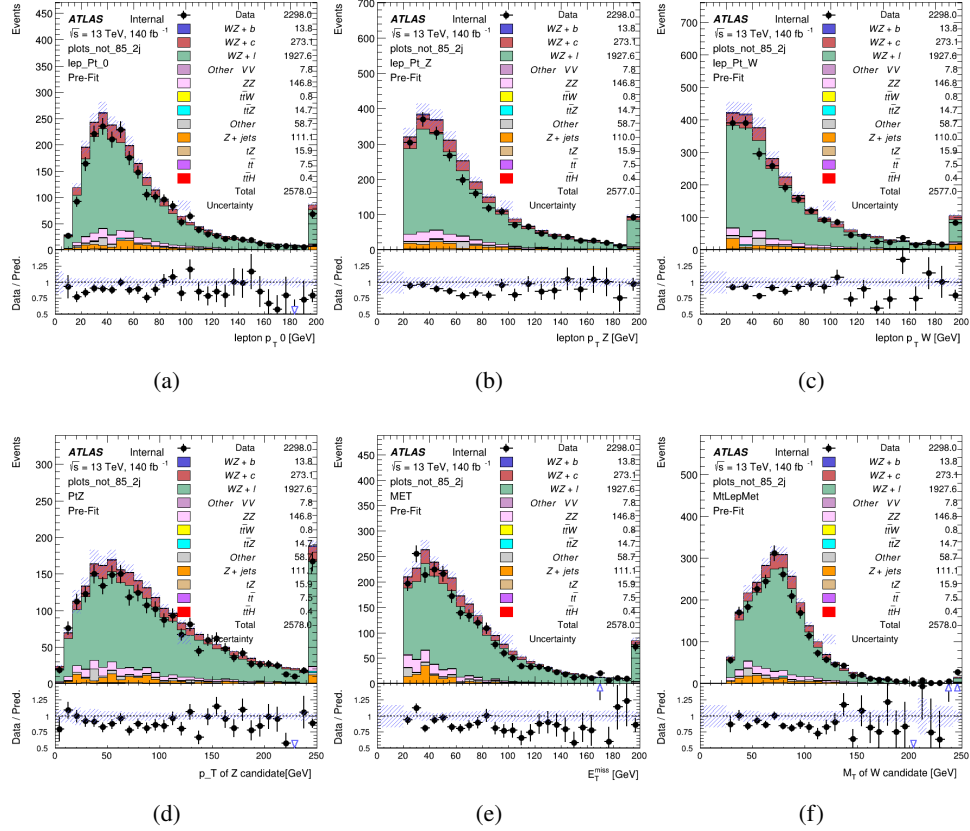


Figure 11: Comparisons between the data and MC distributions in the preselection region for (a) the p_T of the opposite sign lepton, (b) the p_T of the other lepton from the Z candidate, (c) the p_T of the lepton from the W candidate, (d) the p_T of the Z candidate, (e) the E_T^{miss} , and (f) the m_T of the W candidate.

WZ Fit Region - 2j 77-85% WP

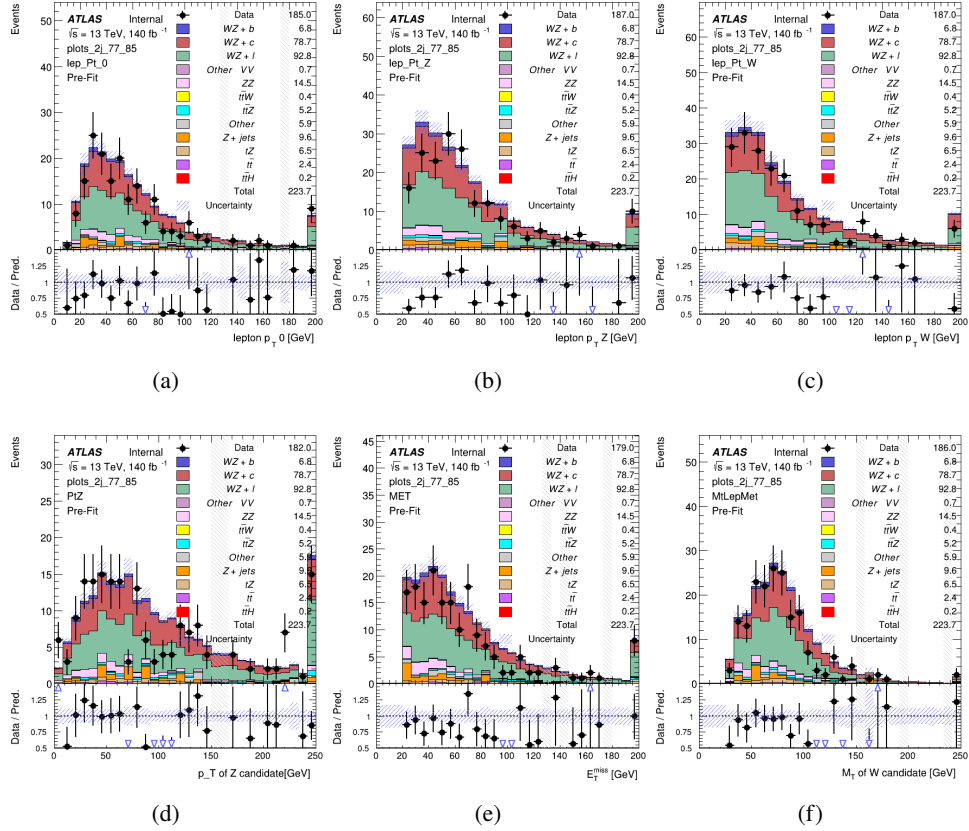


Figure 12: Comparisons between the data and MC distributions in the preselection region for (a) the p_T of the opposite sign lepton, (b) the p_T of the other lepton from the Z candidate, (c) the p_T of the lepton from the W candidate, (d) the p_T of the Z candidate, (e) the E_T^{miss} , and (f) the m_T of the W candidate.

WZ Fit Region - 2j 70-77% WP

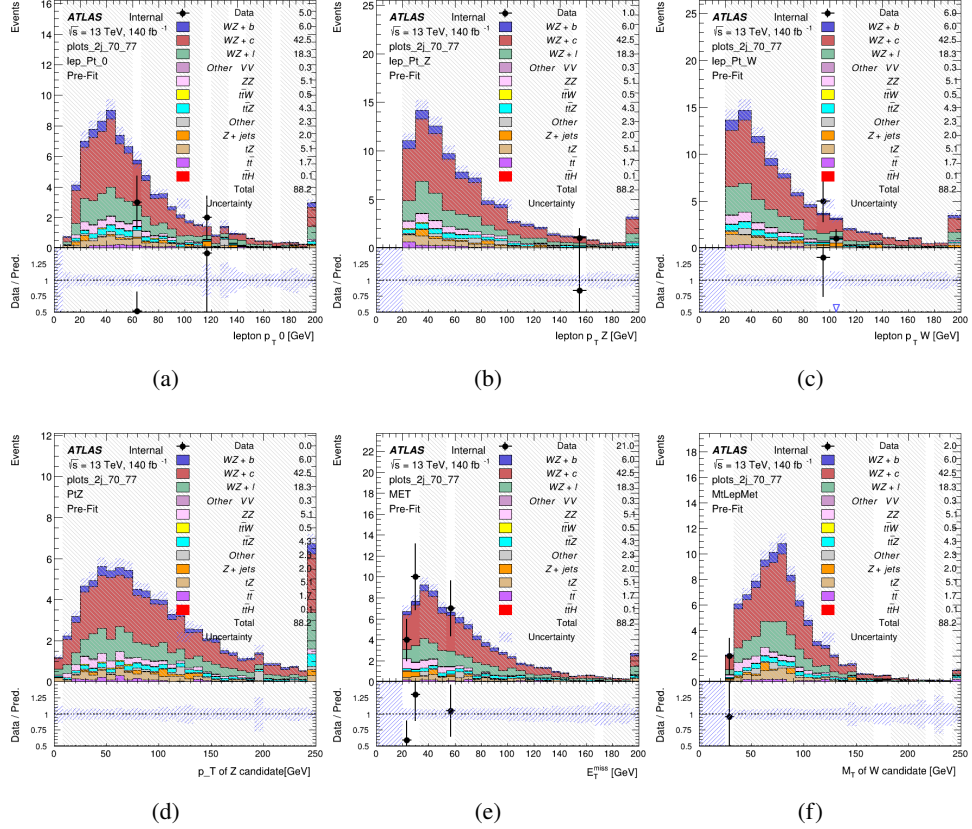


Figure 13: Comparisons between the data and MC distributions in the preselection region for (a) the p_T of the opposite sign lepton, (b) the p_T of the other lepton from the Z candidate, (c) the p_T of the lepton from the W candidate, (d) the p_T of the Z candidate, (e) the E_T^{miss} , and (f) the m_T of the W candidate.

WZ Fit Region - 2j 60-70% WP

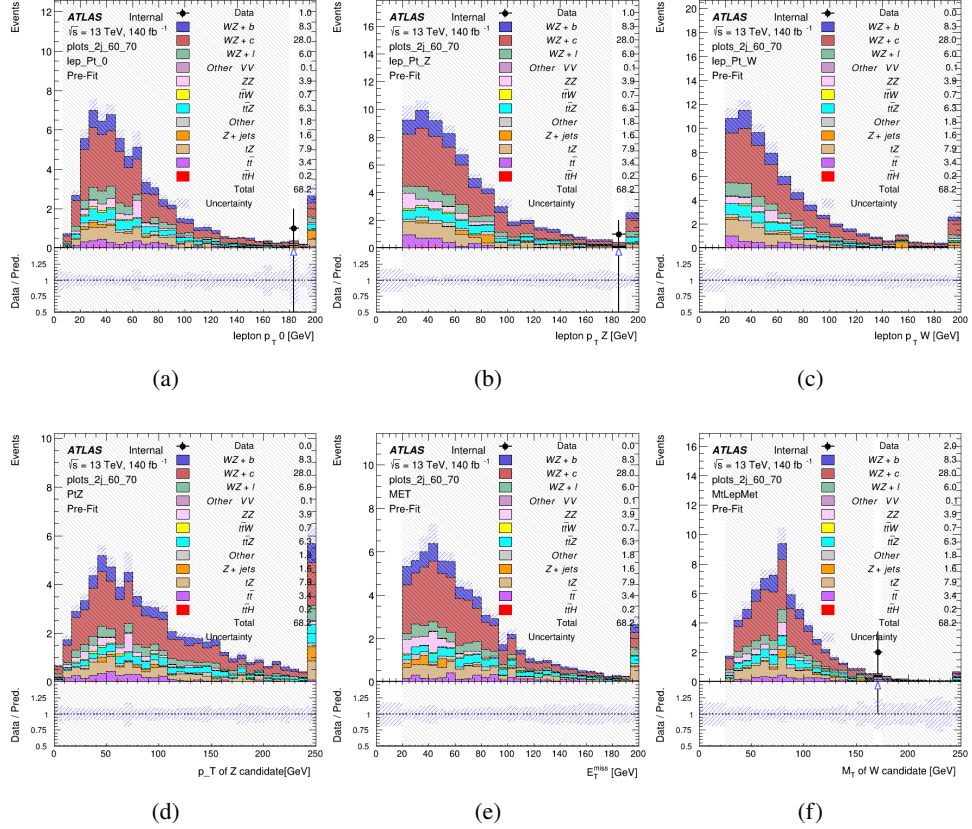


Figure 14: Comparisons between the data and MC distributions in the preselection region for (a) the p_T of the opposite sign lepton, (b) the p_T of the other lepton from the Z candidate, (c) the p_T of the lepton from the W candidate, (d) the p_T of the Z candidate, (e) the E_T^{miss} , and (f) the m_T of the W candidate.

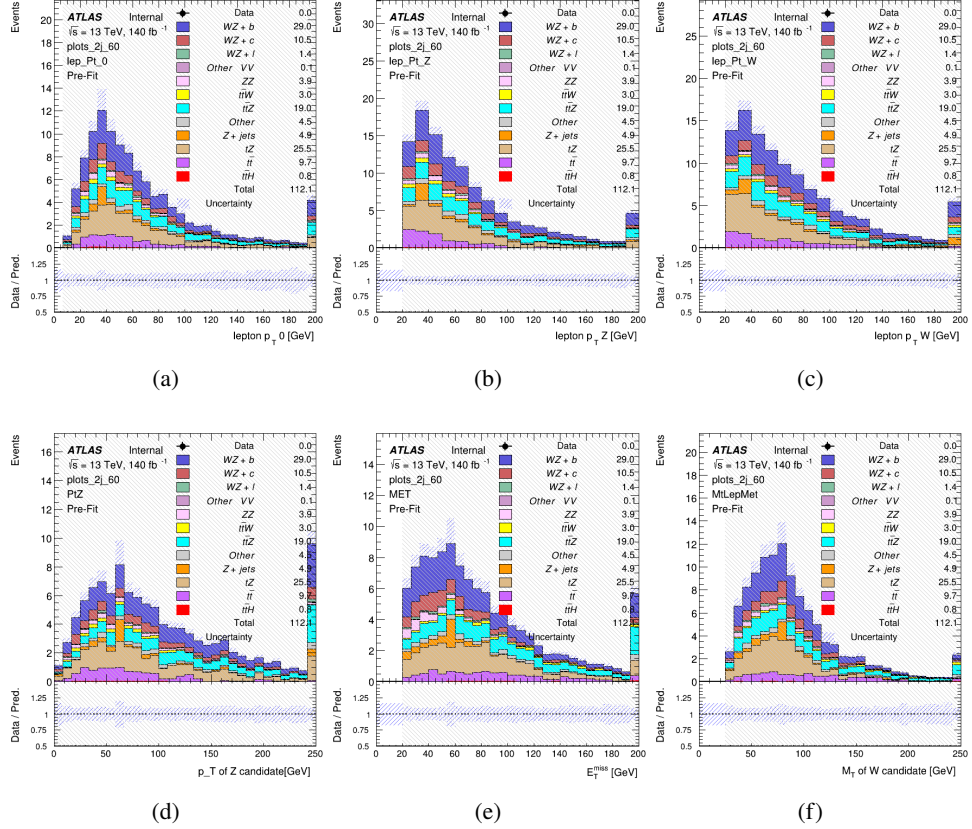
WZ Fit Region - 2j 60% WP

Figure 15: Comparisons between the data and MC distributions in the preselection region for (a) the p_T of the opposite sign lepton, (b) the p_T of the other lepton from the Z candidate, (c) the p_T of the lepton from the W candidate, (d) the p_T of the Z candidate, (e) the E_T^{miss} , and (f) the m_T of the W candidate.

WZ Fit Region - tZ-CR-2j

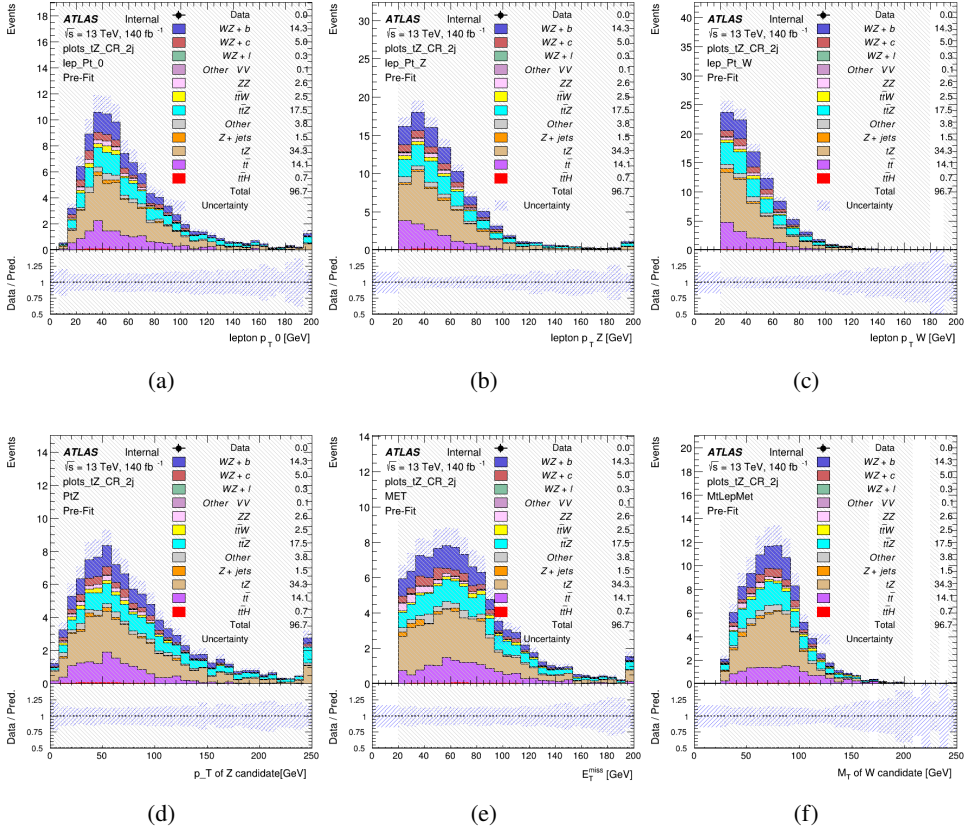


Figure 16: Comparisons between the data and MC distributions in the preselection region for (a) the p_T of the opposite sign lepton, (b) the p_T of the other lepton from the Z candidate, (c) the p_T of the lepton from the W candidate, (d) the p_T of the Z candidate, (e) the E_T^{miss} , and (f) the m_T of the W candidate.

5.3 Non-Prompt Lepton Estimation

Two processes act as sources of non-prompt leptons appear in the analysis: $t\bar{t}$ and $Z+jet$ production both produce two prompt leptons, and each contribute to the 31 region when an additional non-prompt lepton appears in the event. The contribution of these processes is estimated with Monte Carlo simulations, which are validated using enriched validation regions.

5.3.1 $t\bar{t}$ Validation

$t\bar{t}$ events can produce two prompt leptons from the decay of each of the tops. These top decays produce two b-quarks, the decay of which can produce additional non-prompt leptons, which occasionally pass the event preselection. In order to validate that the Monte Carlo accurately

280 simulates this process accurately, the MC prediction in a non-prompt $t\bar{t}$ enriched validation
281 region is compared to data.

282 The $t\bar{t}$ validation region is similar to the preselection region - three leptons meeting the criteria
283 described in section 5 are required, and the requirements on E_T^{miss} remain the same. However,
284 the selection requiring a lepton pair form a Z-candidate are reversed. Events where the invariant
285 mass of any two opposite sign, same flavor leptons falls within 10 GeV of 91.2 GeV are rejected.
286 This ensures the $t\bar{t}$ validation region is orthogonal to the preselection region.

287 Further, because the jet multiplicity of $t\bar{t}$ events tends to be higher than WZ, the number of jets
288 in each event is required to be greater than 1. As b-jets are almost invariably produced from top
289 decays, at least one b-tagged jet passing the 70% DL1r WP in each event is required. Various
290 kinematic plots of this region are shown in figure 17.

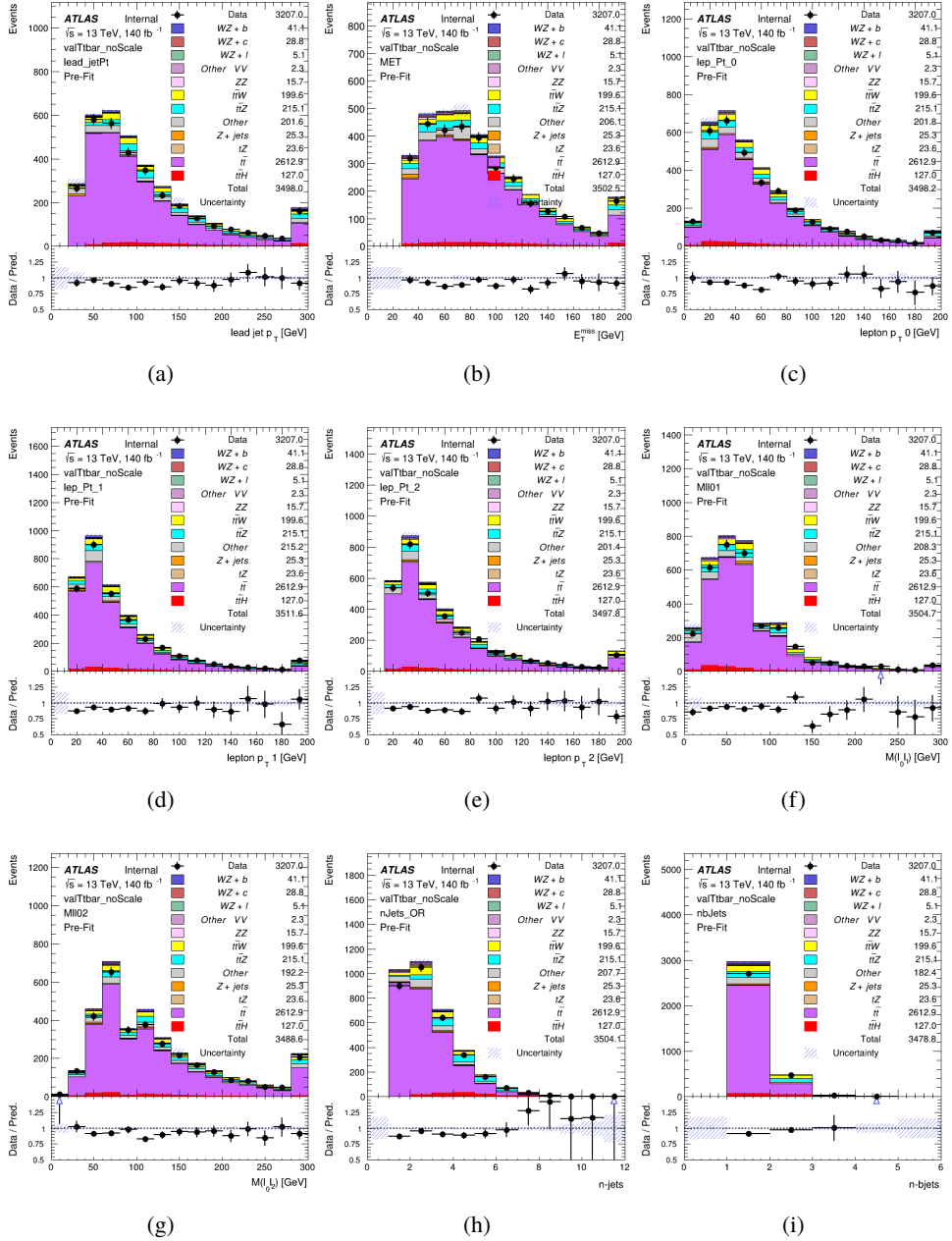


Figure 17: Comparisons between the data and MC distributions in the $t\bar{t}$ validation region for (a) the p_T of the leading jet, (b) the missing transverse energy, (c) the p_T of lepton 0, (d) p_T of lepton 1, (e) p_T of lepton 2, (f) the invariant mass of leptons 0 and 1, (g) the invariant mass of leptons 0 and 2, (h) the number of jets, (i) the number of b-tagged jets.

291 The shape of each distribution agrees quite well between data and MC, with a constant offset
 292 between the two. This is accounted for by applying a constant correction factor of 0.883 to the $t\bar{t}$

293 MC prediction. Plots showing the kinematics of the $t\bar{t}$ VR after this correction factor has been
 294 applied are shown in figure 18.

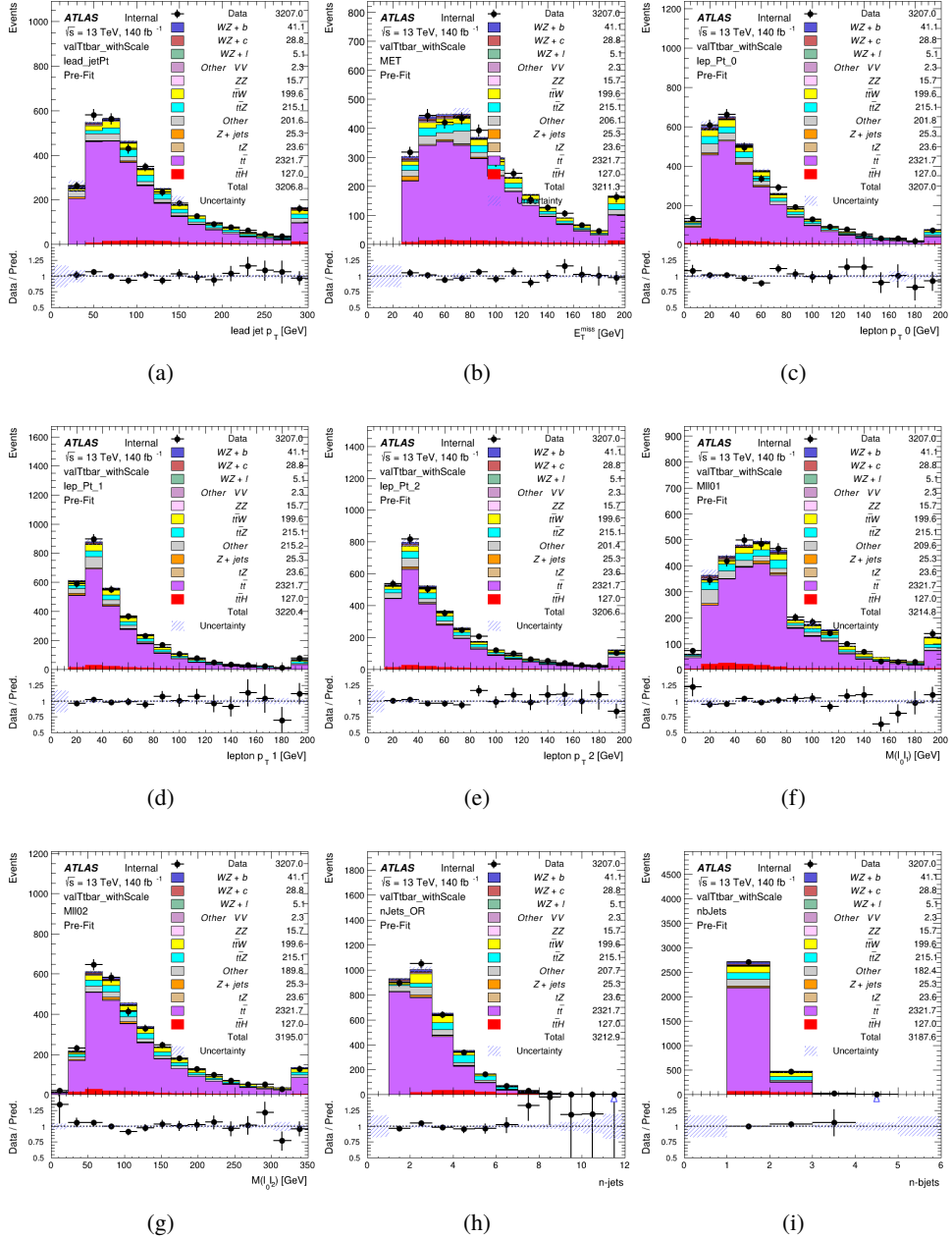


Figure 18: Comparisons between the data and MC distributions in the $t\bar{t}$ validation region after the correction factor has been applied for (a) the p_T of the leading jet, (b) the missing transverse energy, (c) the p_T of lepton 0, (d) p_T of lepton 1, (e) p_T of lepton 2, (f) the invariant mass of leptons 0 and 1, (g) the invariant mass of leptons 0 and 2, (h) the number of jets, (i) the number of b-tagged jets.

295 The modeling is further validated by looking at the yield in the $t\bar{t}$ VR for each DL1r WP, giving
 296 a clearer correspondence to the signal regions used in the fit. Each region shown in figure 22
 297 requires one or more jets pass the listed WP, with no jets passing the next highest WP.

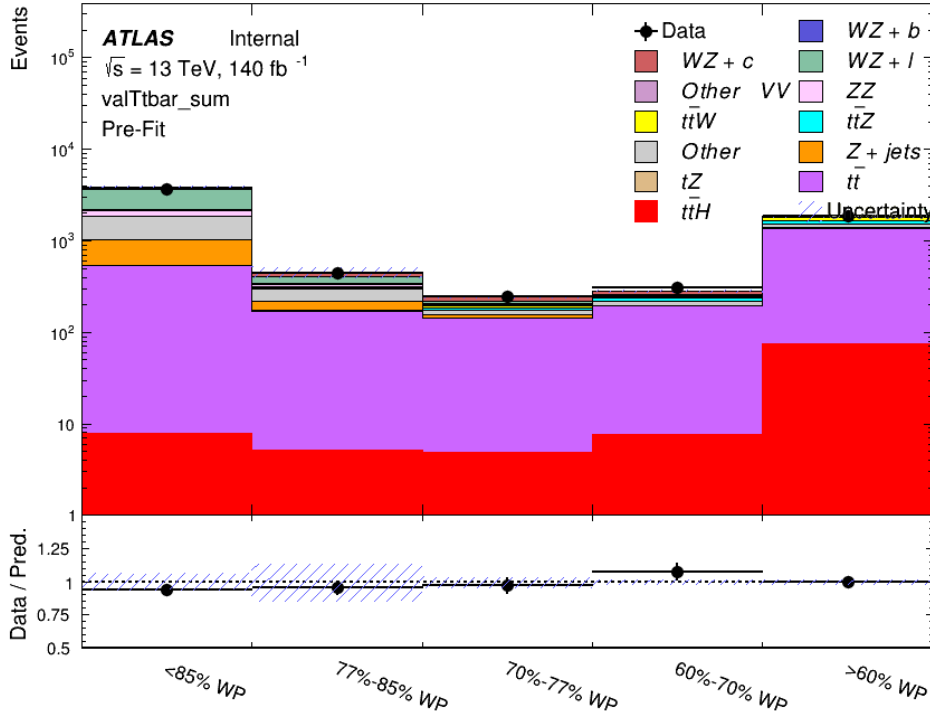


Figure 19: Data and MC comparisons for each DL1r WP for both 1-jet and 2-jet regions, after the $t\bar{t}$ VR selection and correction factor have been applied

298 As data and MC are found to agree within 10% for each of these working points, a 10% systematic
 299 uncertainty on the $t\bar{t}$ prediction is included for the analysis.

300 5.3.2 Z+jets Validation

301 Similar to $t\bar{t}$, a non-prompt Z+jets validation region is produced in order to validate the MC
 302 predictions. The lepton requirements remain the same as the preselection region. Because no
 303 neutrinos are present for this process, the E_T^{miss} cut is reversed, requiring $E_T^{\text{miss}} < 30 \text{ GeV}$. This
 304 also ensures this validation region is orthogonal to the preselection region. Further, the number
 305 of jets in each event is required to be greater than or equal to one. Various kinematic plots of this
 306 region are shown below. The general agreement between data and MC in each of these suggests
 307 that the non-prompt contribution of Z+jets is well modeled by Monte Carlo.

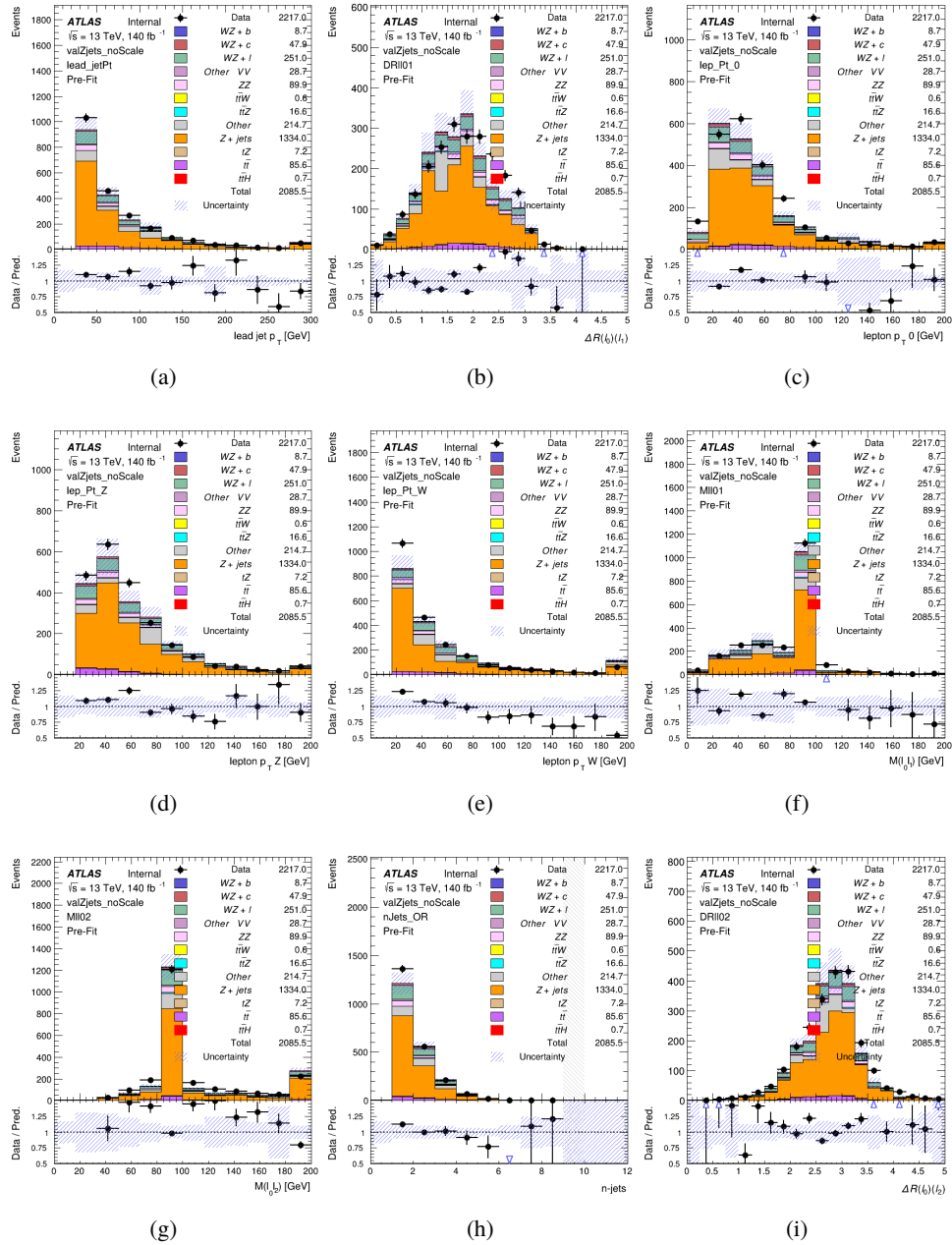


Figure 20: Comparisons between the data and MC distributions in the Z+jets validation region for (a) the p_T of the leading jet, (b) ΔR between leptons 0 and 1, (c) the p_T of lepton 0, (d) p_T of SS lepton from the Z candidate, (e) p_T of the SS lepton from the W candidate, (f) the invariant mass of leptons 0 and 1, (g) the invariant mass of leptons 0 and 2, (h) the number of jets, (i) ΔR between leptons 0 and 2. Includes only statistical uncertainties

308 While there is general agreement between data and MC within statistical uncertainty, the shape

³⁰⁹ of the p_T spectrum of the lepton from the W is found to differ. To account for this discrepancy,
³¹⁰ a variable correction factor is applied to Z+jets. χ^2 minimization of the lepton 2 p_T spectrum is
³¹¹ performed to derive a correction factor of $1.53 - 6.6 * 10^{-6}(\text{lep_Pt_W})$. Kinematic plots of the
³¹² Z + jets validation region after this correction factor has been applied are shown in figure 21.

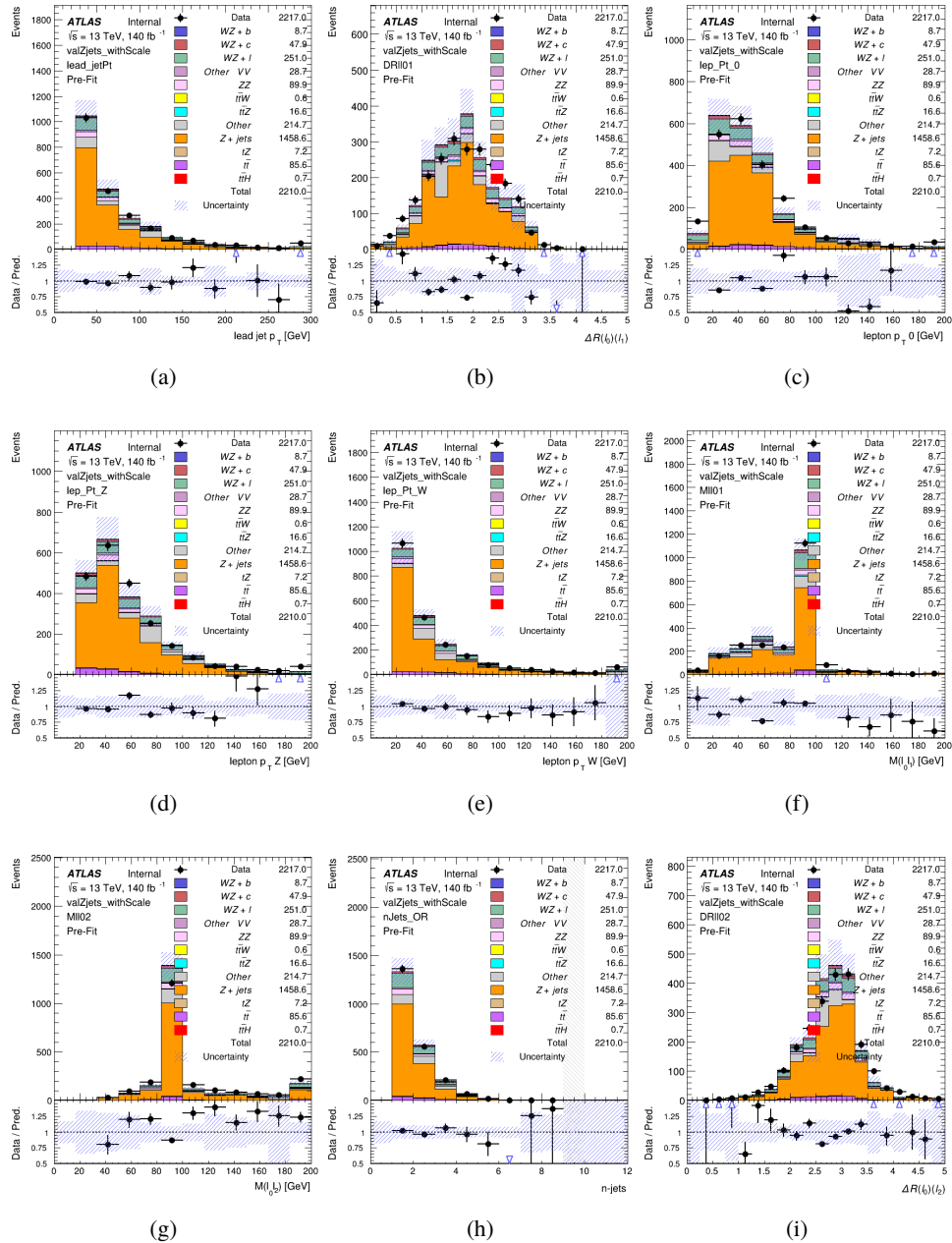


Figure 21: Comparisons between the data and MC distributions in the $Z + \text{jets}$ validation region after the correction factor has been applied for (a) the p_T of the leading jet, (b) ΔR between leptons 0 and 1, (c) the p_T of lepton 0, (d) p_T of SS lepton from the Z candidate, (e) p_T of the SS lepton from the W candidate, (f) the invariant mass of leptons 0 and 1, (g) the invariant mass of leptons 0 and 2, (h) the number of jets, (i) ΔR between leptons 0 and 2

313 The modeling is further validated by looking at the yield in the $Z + \text{jets}$ VR for each DL1r WP,

314 giving a clearer correspondence to the signal regions used in the fit. Each region shown in figure
 315 22 requires one or more jets pass the listed WP, with no jets passing the next highest WP.

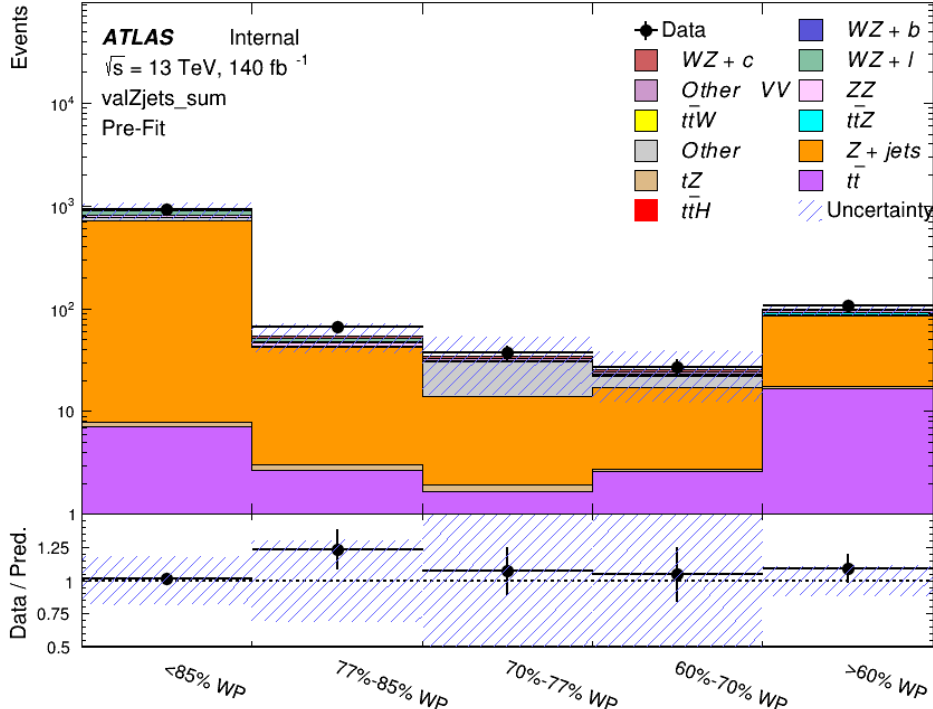


Figure 22: Data and MC comparisons for each DL1r WP for both 1-jet and 2-jet regions, after the Z+jets VR selection and correction factor have been applied

316 For each of the b-tagging working points considered, the data falls within 20% of the MC
 317 prediction once this correction factor has been applied. Therefore, a 20% systematic uncertainty
 318 is applied to Z + jets in the analysis.

319 6 tZ Interference Studies and Separation Multivariate Analysis

320 Because tZ produces a final state identical to signal, it represents a predominant background in
 321 the most signal enriched regions. That is, the region with one jet passing the 60% DL1r WP.
 322 Therefore, a boosted decision tree (BDT) algorithm is trained using TMVA [10] to separate WZ
 323 + heavy flavor from tZ.

324 Separation between tZ and WZ + heavy flavor is achieved in part by reconstructing the invariant
 325 mass of the top candidate, which clusters more closely to the top mass for tZ than WZ + heavy
 326 flavor.

327 The result of this BDT is used to create a tZ enriched region in the fit, reducing its impact on the
 328 measurement of WZ + heavy flavor.

329 **6.1 Top Mass Reconstruction**

330 The reconstruction of the top mass follows the procedure described in detail in section 6.1 of
 331 [11]. The mass of the top quark candidate is reconstructed from the jet, the lepton not included
 332 in the Z-candidate, and a reconstructed neutrino. In the case that there is one jet in the event,
 333 there is only possible b-jet candidate. For events with two jets, the jet with the highest DL1r
 334 score is used.

335 The neutrino from the W decay is expected to be the only source of E_T^{miss} . Therefore, the E_T
 336 and ϕ of the neutrino are taken from the E_T^{miss} measurement. This leaves the z-component of
 337 the neutrino momentum, p_{vz} as the only unknown.

338 This unknown is solved for by taking the combined invariant mass of the lepton and neutrino to
 339 give the invariant mass of the W boson:

$$340 \quad (p_l + p_\nu)^2 = m_W^2$$

341 Expanding this out into components, this equation gives:

$$342 \quad \sqrt{p_{Tv}^2 + p_{zv}^2} E_l = \frac{m_w^2 - m_l^2}{2} + p_{Tv}(p_{lx} \cos\phi_\nu + p_{ly} \sin\phi_\nu) + p_{lz} p_{vz}$$

343 This equation gives two solutions for p_{vz} . For cases where only one of these solutions is real,
 344 that is taken as the value of p_{vz} . For instances with two real solutions, the one which is shown
 345 to be correct in the largest fraction of simulations is taken. For cases when no real solution is
 346 found, often because of detector effects, the value of E_T^{miss} is varied in decreasing increments of
 347 100 MeV until a real solution is found.

348 The reconstructed top mass distribution for tZ and WZ + b can be seen in figure 23.

349 **6.2 tZ BDT**

350 A Boosted Decision Tree (BDT), specifically XGBoost [xgboost_cite], is used to provide separa-
 351 tion between tZ and WZ+b. The following kinematic variables are used as inputs:

- 352 • The invariant mass of the reconstructed top candidate
- 353 • p_T of each of the leptons, jet
- 354 • The invariant mass of each combination of lepton pairs, $M(l\bar{l})$
- 355 • E_T^{miss}

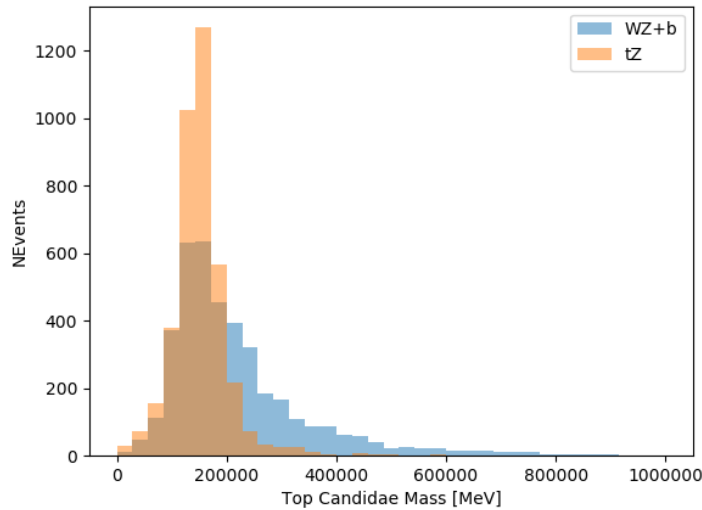


Figure 23: Reconstructed top mass distributions for tZ and WZ + b, measured in MeV.

- 356 • Distance between each combination of leptons, $\Delta R(ll)$
- 357 • Distance between each lepton and the jet, $\Delta R(lj)$

358 The training samples included only events meeting the requirements of the 1-jet, >60% region,
 359 i.e. passing all the selection described in section 5 and having exactly one jet which passes the
 360 tightest (60%) DL1r working point.

361 The distributions of a few of these features for both signal and background is shown in figure
 362 24.

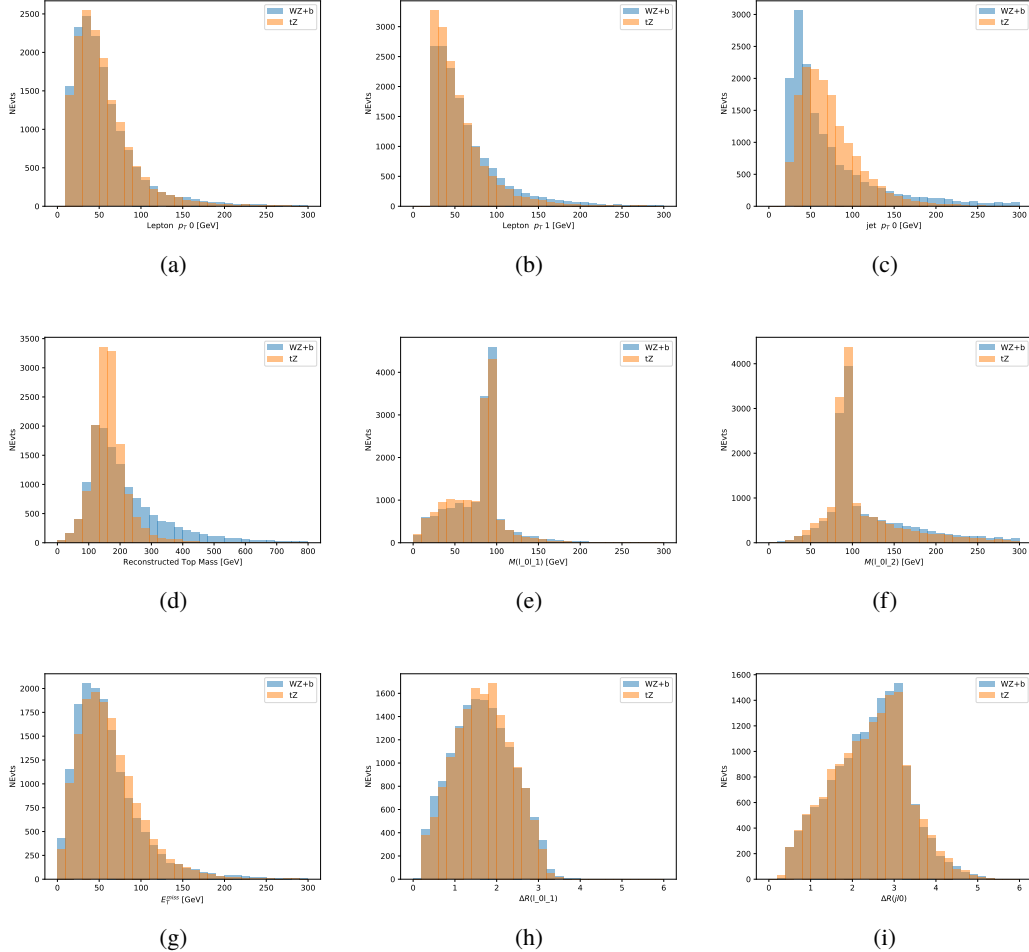


Figure 24: Distribution of input features of the BDT for signal (WZ) and background (tZ). Both are scaled to an equal number of events. (a), (b) and (c) show the p_T of lepton 0, lepton 1, and the jet, (d) show the reconstructed top mass, (e) and (f) show the invariant mass of leptons 0 and 1, leptons 0 and 2. (g) shows the E_T^{miss} of each event. (h) and (i) show the ΔR between lepton 0 and lepton 1, and the jet.

363 A sample of 20,000 background (tZ) and signal (WZ+b) Monte Carlo events are used to train
 364 the BDT. And additional 5,000 events are reserved for testing the model, in order to prevent
 365 over-fitting. A total of 750 decision trees with a maximum depth of 6 branches are used to build
 366 the model. These parameters are chosen empirically, by training several models with different
 367 parameters and selecting the one that gave the best separation for the test sample.

368 The results of the BDT training are shown in figure 25. The output scores for both signal and
 369 background events is shown on the left. The right shows the receiving operating characteristic
 370 (ROC) curve that results from the MVA. The ROC curve represents the background rejection
 371 as a function of signal efficiency, where each point on the curve represents a different response

372 score. The ROC curve of the BDT is compared to the performance of using an optimal set of flat
 373 selections on the same set of input variables.

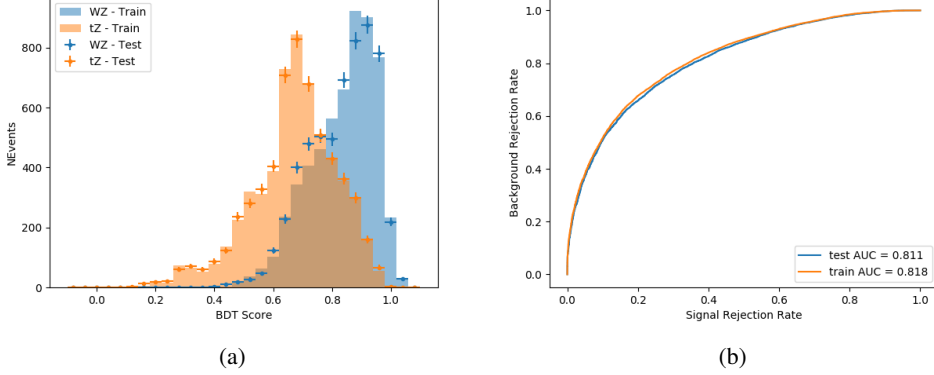


Figure 25: Distribution of the BDT response for signal and background events on the left, the ROC curve for the BDT on the right.

374 The relative important of each input feature in the model, measured by how often they appeared
 375 in the decision trees, is shown in figure 26.

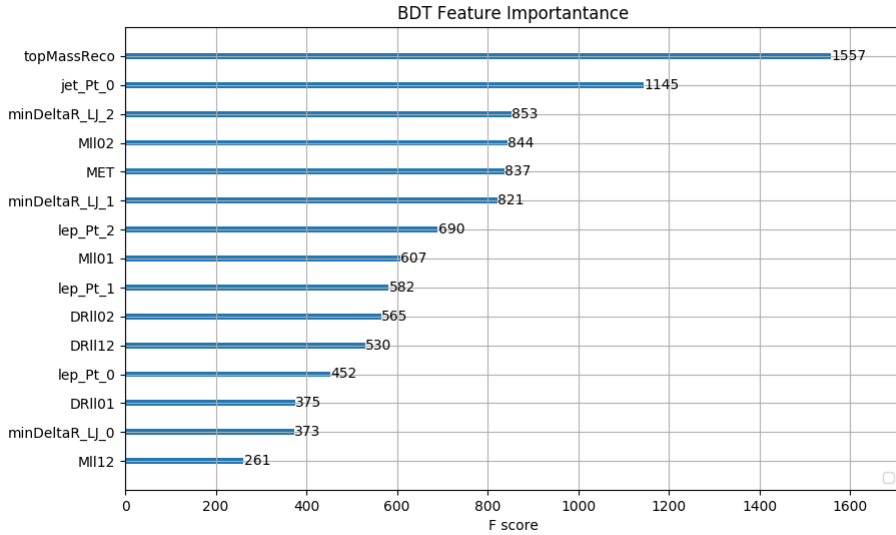


Figure 26: Relative importance of each input feature in the model.

376 These results suggest that some amount of separation can be achieved between these two pro-
 377 cesses, with a high BDT score selecting a set of events that is pure in $WZ + b$. A BDT score

378 of 0.725 is selected as a cutoff, where events with scores higher than this form a signal enriched
 379 region, and events with scores lower than this form a tZ control region. This cutoff is selected by
 380 varying the value of this cutoff in stat-only Asimov fits, and selecting the value that minimizes
 381 the statistical uncertainty on WZ + b.

382 7 Systematic Uncertainties

383 The systematic uncertainties that are considered are summarized in table 8. These are imple-
 384 mented in the fit either as a normalization factors or as a shape variation or both in the signal
 385 and background estimations. The numerical impact of each of these uncertainties is outlined in
 386 section 8.

Table 8: Sources of systematic uncertainty considered in the analysis.

Systematic uncertainty	Components
Luminosity	1
Pileup reweighting	1
Physics Objects	
Electron	6
Muon	15
Jet energy scale	28
Jet energy resolution	8
Jet vertex fraction	1
Jet flavor tagging	131
E_T^{miss}	3
Total (Experimental)	194
Signal Modeling	
Shape modelling	3
Renormalization and factorization scales	5
Background Modeling	
Cross section	15
Renormalization and factorization scales	12
Total (Signal and background modeling)	35
Total (Overall)	229

387 The uncertainty in the combined integrated luminosity is derived from a calibration of the
 388 luminosity scale performed for 13 TeV proton-proton collisions [12], [**LUCID2**].

389 The experimental uncertainties are related to the reconstruction and identification of light leptons
 390 and b-tagging of jets, and to the reconstruction of E_T^{miss} . The sources which contribute to the
 391 uncertainty in the jet energy scale (JES) [13] are decomposed into uncorrelated components and

392 treated as independent sources in the analysis. The CategoryReduction model is used to account
393 for JES uncertainties, which decomposes the uncertainties into 30 nuisance parameters included
394 in the fit. The SimpleJER model is used to account for jet energy resolution (JER) uncertainties,
395 and 8 JER uncertainty components unclued as NPs in the fit.

396 The uncertainties in the b-tagging efficiencies measured in dedicated calibration analyses [14] are
397 also decomposed into uncorrelated components. The large number of components for b-tagging
398 is due to the calibration of the distribution of the MVA discriminant.

399 The full list of systematic uncertainties considered in the analysis is summarized in tables 9, 10
400 and 11.

401

Experimental Systematics on Leptons and E_T^{miss}			
Type	Description	Systematics Name	Application
Trigger			
Scale Factors	Trigger Efficiency	lepSFTrigTight_MU(EL)_SF_Trigger_STAT(SYST)	Event Weight
Muons			
Efficiencies	Reconstruction and Identification	lepSFObjTight_MU_SF_ID_STAT(SYST)	Event Weight
	Isolation	lepSFObjTight_MU_SF_Isol_STAT(SYST)	Event Weight
	Track To Vertex Association	lepSFObjTight_MU_SF_TTVA_STAT(SYST)	Event Weight
p_T Scale	p_T Scale	MUONS_SCALE	p_T Correction
Resolution	Inner Detector Energy Resolution	MUONS_ID	p_T Correction
	Muon Spectrometer Energy Resolution	MUONS_MS	p_T Correction
Electrons			
Efficiencies	Reconstruction	lepSFObjTight_EL_SF_ID	Event Weight
	Identification	lepSFObjTight_EL_SF_Reco	Event Weight
	Isolation	lepSFObjTight_EL_SF_Isol	Event Weight
Scale Factor	Energy Scale	EG_SCALE_ALL	Energy Correction
Resolution	Energy Resolution	EG_RESOLUTION_ALL	Energy Correction
E_T^{miss}			
Soft Tracks Terms	Resolution	MET_SoftTrk_ResoPerp	p_T Correction
	Resolution	MET_SoftTrk_ResoPara	p_T Correction
	Scale	MET_SoftTrk_ScaleUp	p_T Correction
	Scale	MET_SoftTrk_ScaleDown	p_T Correction

Table 9: Summary of experimental systematics considered for leptons and E_T^{miss} . Includes type, description, name of systematic as used in the fit, and mode of application. The mode of application indicates the systematic evaluation, e.g. as an overall event re-weighting (Event Weight) or rescaling (p_T Correction).

Experimental Systematics on Jets			
Type	Origin	Systematics Name	Application
Jet Vertex Tagger		JVT	Event Weight
Energy Scale	Calibration Method	JET_21NP_ JET_EffectiveNP_1-19	p_T Correction p_T Correction
	η inter-calibration	JET_EtaIntercalibration_Modelling JET_EtaIntercalibration_NonClosure JET_EtaIntercalibration_TotalStat	p_T Correction p_T Correction p_T Correction
	High p_T jets	JET_SingleParticle_HighPt	p_T Correction
	Pile-Up	JET_Pileup_OffsetNPV JET_Pileup_OffsetMu JET_Pileup_PtTerm JET_Pileup_RhoTopology	p_T Correction p_T Correction p_T Correction p_T Correction
	Non Closure	JET_PunchThrough_MC15	p_T Correction
	Flavour	JET_Flavor_Response JET_BJES_Response JET_Flavor_Composition	p_T Correction p_T Correction p_T Correction
Resolution		JET_JER_SINGLE_NP	Event Weight

Table 10: Jet systematics take into account effects of jets calibration method, η inter-calibration, high p_T jets, pile-up, and flavor response. They are all diagonalised into effective parameters.

Experimental Systematics on b-tagging		
Type	Origin	Systematic Name
Scale Factors	DL1r b-tagger efficiency on b originated jets in bins of η	DL1r_Continuous_EventWeight_B0-29
	DL1r b-tagger efficiency on c originated jets in bins of η	DL1r_Continuous_EventWeight_C0-19
	DL1r b-tagger efficiency on light flavoured originated jets in bins of η and p_T	DL1r_Continuous_EventWeight_Light0-79
	DL1r b-tagger extrapolation efficiency	DL1r_Continuous_EventWeight_extrapolation DL1r_Continuous_EventWeight_extrapolation_from_charm

Table 11: Summary of experimental systematics to be included for b-tagging of jets in the analysis, using the continuous DL1r tagging algorithm. All of the b-tagging related systematics are applied as event weights. From left: type, description, and the name of systematic used in the fit.

- 402 Theoretical uncertainties applied to MC predictions, including cross section, PDF, and scale
 403 uncertainties are taken from theory calculations, with the exception of non-prompt and diboson
 404 backgrounds. The cross-section uncertainty on tZ is taken from [tZ_paper]. Derivation of the
 405 non-prompt background uncertainties, Z+jets and tt>, are explained in detail in section 5.3.
 406 The other VV + heavy flavor processes (namely VV+b and VV+charm, which primarily consist
 407 of ZZ events) are also poorly understood, because these processes involve the same physics as
 408 WZ + heavy flavor, and have also not been measured. Therefore, a conservative 50% uncertainty
 409 is applied to those samples. While this uncertainty is large, it is found to have little impact on
 410 the significance of the final result.
 411 The theory uncertainties applied to the predominate background estimates are summarized in
 412 table 12.

Process	X-section [%]
tZ	X-sec: ± 15.2 QCD Scale: $^{+5.2}_{-1.3}$ PDF($+\alpha_S$): ± 1.2
t <bar>t} H (aMC@NLO+Pythia8)</bar>	QCD Scale: $^{+5.8}_{-9.2}$ PDF($+\alpha_S$): ± 3.6
t <bar>t} Z (aMC@NLO+Pythia8)</bar>	QCD Scale: $^{+9.6}_{-11.3}$ PDF($+\alpha_S$): ± 4
t <bar>t} W (aMC@NLO+Pythia8)</bar>	QCD Scale: $^{+12.9}_{-11.5}$ PDF($+\alpha_S$): ± 3.4
VV + b/charm (Sherpa 2.2.1)	± 50
VV + light (Sherpa 2.2.1)	± 6
t <bar>t}</bar>	± 10
Z + jets	± 20
Others	± 50

Table 12: Summary of theoretical uncertainties for MC predictions in the analysis.

413 Additional signal uncertainties are estimated by comparing estimates from the nominal Sherpa
 414 WZ samples with alternate WZ samples generated with Powheg+PYTHIA8 (DSID 361601).
 415 The shape of the templates used in the fit are compared between these two samples for WZ + b,
 416 WZ + charm and WZ + light, as shown in figures 27 and 28. Each of these plots are normalized
 417 to unity in order to capture differences in shape.

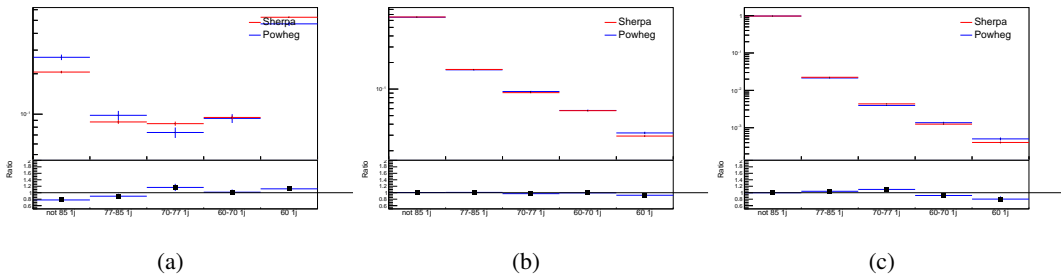


Figure 27: Comparison between Sherpa and Powheg predictions of the distribution of (a) WZ + b, (b) WZ + charm, and (c) WZ + light among the various b-tag WPs used in the 1-jet fit.

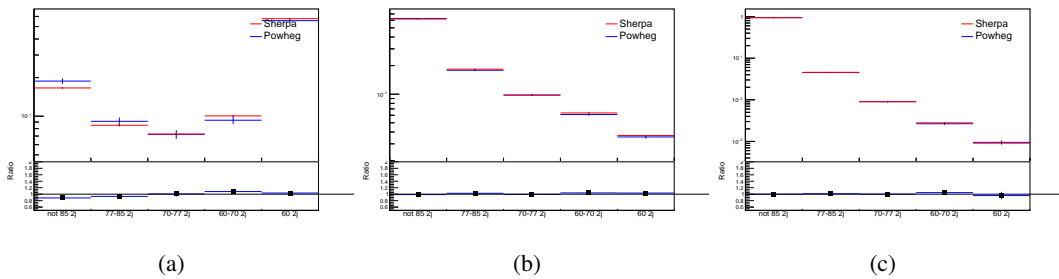


Figure 28: Comparison between Sherpa and Powheg predictions of the distribution of (a) WZ + b, (b) WZ + charm, and (c) WZ + light among the various b-tag WPs used in the 2-jet fit.

⁴¹⁸ Separate systematics are included in the fit for WZ + b, WZ + charm and WZ + light, where
⁴¹⁹ the distribution among each of the fit regions is varied based on the prediction of the Powheg
⁴²⁰ sample.

8 Results

A separate maximum-likelihood fit is performed over the 1-jet and 2-jet fit regions in order to extract the best-fit value of the WZ + b-jet and WZ + charm jet contributions. The WZ + b, WZ + charm and WZ + light contributions are allowed to float, with the remaining background contributions are held fixed. **The current fit strategy treats the WZ + b-jet contribution as the parameter of interest, with the normalization of the WZ + charm and the WZ + light contributions taken as systematic uncertainties. This could however be adjusted, depending on whether it is decided the goal of the analysis should be to measure WZ+b specifically or WZ + heavy flavor overall.** The result of the fit is used to extract the cross-section of WZ + heavy-flavor production.

431 A maximum likelihood fit to data is performed simultaneously in the regions described in section
 432 5. The parameters μ_{WZ+b} , $\mu_{WZ+charm}$, $\mu_{WZ+light}$, where $\mu = \sigma_{\text{observed}}/\sigma_{\text{SM}}$, are extracted
 433 from the fit.

The Asimov fit for 1-jet events gives an expected μ value of $1.00^{+0.37}_{-0.35}(\text{stat})^{+0.24}_{-0.22}(\text{sys})$ for WZ + b. The fitted cross-section modifiers for WZ + charm and WZ + light are $1.00 \pm 0.17 \pm 0.15$ and $1.00 \pm 0.04 \pm 0.07$, respectively.

437 The expected cross-section of WZ+b with 1 associated jet obtained from the fit is $1.74^{+0.65}_{-0.61}(\text{stat})^{+0.42}_{-0.37}(\text{sys})$
 438 fb with an expected significance of 2.2σ . The expected cross-section of WZ + charm is measured
 439 to be $14.6 \pm 2.5(\text{stat}) \pm 2.1(\text{sys})$ fb, with a correlation of -0.23.

For 2-jet events, the fit gives an expected μ value of $1.00^{+0.34}_{-0.33}(\text{stat})^{+0.29}_{-0.28}(\text{sys})$ for WZ + b. The fitted cross-section modifiers for WZ + charm and WZ + light are $1.00 \pm 0.17 \pm 0.15$ and $1.00 \pm 0.04 \pm 0.08$, respectively.

⁴⁴³ The expected $WZ + b$ cross-section in the 2-jet region is $2.46^{+0.83}_{-0.81}(\text{stat})^{+0.0.73}_{-0.68}(\text{sys}) \text{ fb}$ with
⁴⁴⁴ an expected significance of 2.6σ . The 2-jet expected cross-section of $WZ + \text{charm}$ is $12.7 \pm 2.2(\text{stat}) \pm 2.0(\text{sys}) \text{ fb}$, and the correlation between $WZ + \text{charm}$ and $WZ + b$ is -0.26.

⁴⁴⁶ 8.1 1-jet Fit Results

⁴⁴⁷ The results of the fit are currently blinded.

⁴⁴⁸ The pre-fit yields in each of the regions used in the fit are shown in table 8.1, and summarized in
⁴⁴⁹ figure 29.

⁴⁵⁰

Sample	1j, <85% WP	1j, 77%-85% WP	1j, 70%-77% WP	1j, 60%-70% WP	1j, >60% WP	tZ CR
$WZ + b$	11 ± 2	4.7 ± 0.5	4.6 ± 0.4	5.1 ± 0.4	24 ± 2	6.0 ± 0.5
$WZ + c$	318 ± 22	81 ± 6	43.1 ± 3.6	25.8 ± 2.6	9.4 ± 1.8	2.9 ± 0.6
$WZ + l$	4020 ± 250	91 ± 13	17 ± 3	4.9 ± 1.6	1.3 ± 0.4	0.2 ± 0.1
Other VV	6.2 ± 0.6	0.2 ± 0.4	0.2 ± 0.04	0.07 ± 0.1	0.1 ± 0.1	0.1 ± 0.2
ZZ	336 ± 26	17.8 ± 2.1	4.3 ± 0.6	1.7 ± 0.5	0.36 ± 0.08	0.10 ± 0.03
$t\bar{t}W$	1.1 ± 0.2	0.2 ± 0.1	0.3 ± 0.1	0.4 ± 0.1	1.5 ± 0.3	0.7 ± 0.2
$t\bar{t}Z$	6.8 ± 1.2	1.4 ± 0.3	1.0 ± 0.2	1.2 ± 0.2	4.4 ± 0.8	3.2 ± 0.6
$Z + \text{jets}$	169 ± 38	8.9 ± 1.9	3.7 ± 0.8	3.3 ± 0.7	3.2 ± 0.7	0.8 ± 0.17
$V + \gamma$	45 ± 28	1.9 ± 2.4	0.1 ± 0.1	0.02 ± 0.01	1.0 ± 0.9	0.02 ± 0.03
tZ	24.3 ± 4.3	5.5 ± 1.1	4.1 ± 0.8	5.9 ± 1.1	10.7 ± 2.0	23 ± 4
tW	1.4 ± 0.8	0.2 ± 0.5	0.0 ± 0.2	0.7 ± 0.6	0.26 ± 0.42	0.39 ± 0.41
WtZ	2.3 ± 1.2	0.6 ± 0.3	0.3 ± 0.21	0.27 ± 0.2	1.1 ± 0.7	0.6 ± 0.5
VVV	12.4 ± 0.5	0.93 ± 0.06	0.35 ± 0.03	0.13 ± 0.02	0.14 ± 0.03	0.02 ± 0.01
VH	40 ± 6	2.6 ± 1.4	0.9 ± 0.8	0.7 ± 0.8	0.5 ± 0.6	0.0 ± 0.0
$t\bar{t}$	12.1 ± 1.6	2.9 ± 0.6	2.5 ± 0.5	2.8 ± 0.5	11.2 ± 1.4	10.9 ± 1.5
$t\bar{t}H$	0.24 ± 0.03	0.05 ± 0.01	0.04 ± 0.01	0.06 ± 0.01	0.20 ± 0.03	0.13 ± 0.02
Total	5010 ± 260	227 ± 24	88 ± 12	57 ± 8	76 ± 16	53 ± 8

Table 13: Pre-fit yields in each of the 1-jet fit regions.

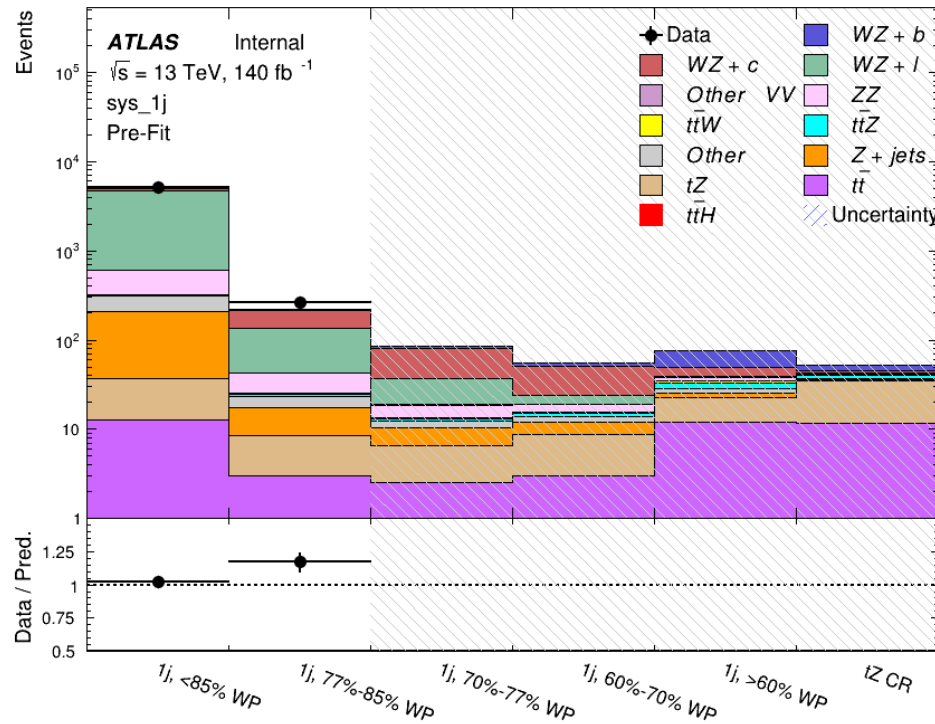


Figure 29: Pre-fit summary of the 1-jet fit regions.

451 The post-fit yields in each region are summarized in figure 8.1.

452

	1j, <85% WP	1j, 77%-85% WP	1j, 70%-77% WP	1j, 60%-70% WP	1j, >60% WP	tZ CR
WZ + b	11 ± 5	4.7 ± 2.0	4.6 ± 2.0	5.1 ± 2.1	24 ± 10	6.0 ± 2.50
WZ + c	320 ± 60	80 ± 14	43 ± 7	26 ± 5	9.4 ± 2.3	2.9 ± 0.7
WZ + l	4020 ± 130	90 ± 11	17.3 ± 2.8	4.9 ± 1.6	1.3 ± 0.4	0.23 ± 0.13
Other VV	6.2 ± 0.6	0.92 ± 0.07	0.02 ± 0.01	0.01 ± 0.01	0.01 ± 0.01	0.01 ± 0.01
ZZ	346 ± 57	19 ± 5	4.3 ± 0.8	2.7 ± 0.5	2.4 ± 0.1	2.1 ± 0.6
t̄tW	1.09 ± 0.21	0.2 ± 0.1	0.1 ± 0.1	0.4 ± 0.1	1.5 ± 0.3	0.1 ± 0.2
t̄tZ	6.8 ± 1.2	1.4 ± 0.3	1.0 ± 0.2	1.2 ± 0.2	4.4 ± 0.7	3.2 ± 0.5
rare Top	0.14 ± 0.04	0.04 ± 0.02	0.04 ± 0.0	0.1 ± 0.03	0.14 ± 0.04	0.15 ± 0.05
t̄tWW	0.04 ± 0.03	0.01 ± 0.02	0.01 ± 0.01	0.01 ± 0.01	0.01 ± 0.02	0.01 ± 0.01
Z + jets	169 ± 37	8.9 ± 1.9	3.7 ± 0.8	3.3 ± 0.7	3.2 ± 0.7	0.8 ± 0.2
W + jets	0.01 ± 0.01					
V + γ	46 ± 28	1.9 ± 2.4	0.1 ± 0.1	0.0 ± 0.2	1.0 ± 0.9	0.0 ± 0.0
tZ	24 ± 4	5.5 ± 1.0	4.1 ± 0.8	5.9 ± 1.1	10.7 ± 1.8	23.3 ± 3.7
tW	1.37 ± 0.82	0.18 ± 0.26	0.01 ± 0.12	0.67 ± 0.64	0.26 ± 0.42	0.39 ± 0.41
WtZ	2.3 ± 1.2	0.6 ± 0.3	0.3 ± 0.2	0.3 ± 0.2	1.1 ± 0.6	0.6 ± 0.3
VVV	12.4 ± 0.4	0.9 ± 0.1	0.4 ± 0.1	0.13 ± 0.02	0.14 ± 0.03	0.02 ± 0.01
VH	40 ± 6	2.6 ± 1.4	0.9 ± 0.8	0.7 ± 0.8	0.4 ± 0.6	0.01 ± 0.01
t̄t	12.1 ± 1.6	2.9 ± 0.6	2.5 ± 0.5	2.8 ± 0.5	11.2 ± 1.5	10.9 ± 1.4
t̄tH	0.24 ± 0.03	0.05 ± 0.01	0.04 ± 0.01	0.06 ± 0.01	0.20 ± 0.03	0.13 ± 0.02
Total	5100 ± 110	227 ± 12	87 ± 6	56.7 ± 4.4	76 ± 9	52.5 ± 4.2

Table 14: Post-fit yields in each of the 1-jet fit regions.

⁴⁵³ A post-fit summary plot of the 1-jet fitted regions is shown in figure 30:

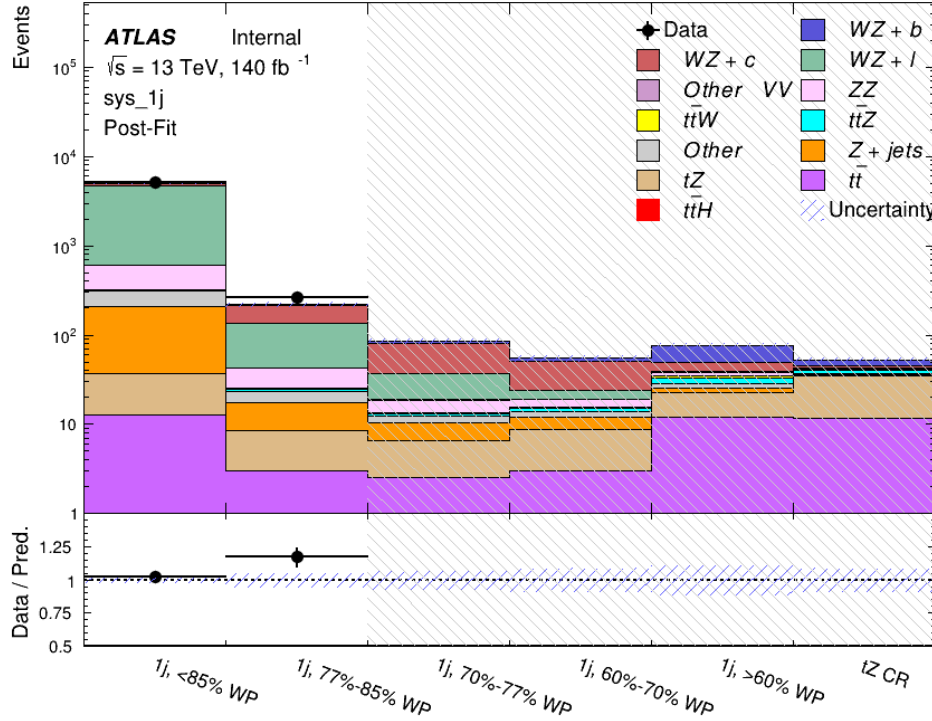


Figure 30: Post-fit summary of the 1-jet fit regions.

454 As described in section 7, there are 226 systematic uncertainties that are considered as NPs in
 455 the fit. These NPs are constrained by Gaussian or log-normal probability density functions. The
 456 latter are used for normalisation factors to ensure that they are always positive. The expected
 457 number of signal and background events are functions of the likelihood. The prior for each NP is
 458 added as a penalty term, decreasing the likelihood as it is shifted away from its nominal value.

459 The impact of each NP is calculated by performing the fit with the parameter of interest held
 460 fixed, varied from its fitted value by its uncertainty, and calculating $\Delta\mu$ relative to the baseline
 461 fit. The impact of the most significant sources of systematic uncertainties is summarized in table
 462 15.

Uncertainty Source	$\Delta\mu$	
WZ + light cross-section	0.13	-0.12
WZ + charm cross-section	-0.10	0.12
Jet Energy Scale	0.08	0.13
tZ cross-section	-0.10	0.10
Jet Energy Resolution	-0.10	0.10
Luminosity	-0.08	0.09
Other Diboson + b cross-section	-0.07	0.07
Flavor tagging	0.05	0.05
t <bar>t} cross-section</bar>	-0.05	0.05
WZ cross-section - QCD scale	-0.04	0.03
Total Systematic Uncertainty	0.28	0.32

Table 15: Summary of the most significant sources of systematic uncertainty on the measurement of WZ + b with exactly one associated jet.

⁴⁶³ The ranking and impact of those nuisance parameters with the largest contribution to the overall
⁴⁶⁴ uncertainty is shown in figure 31.

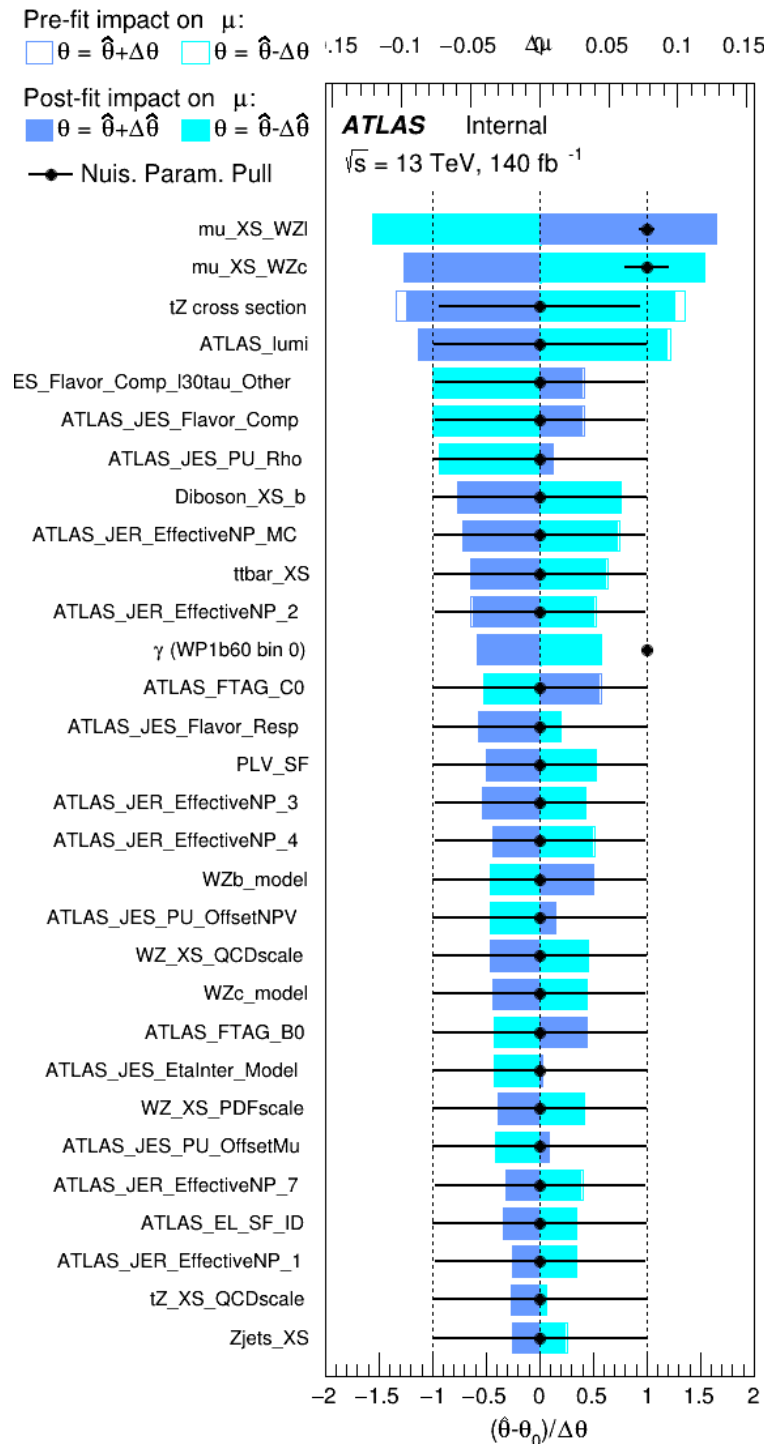


Figure 31: Impact of systematic uncertainties on the signal-strength of $WZ + b$ for events with exactly one jet

465 The large impact of the Jet Energy Scale and Jet Flavor Tagging is unsurprising, as the shape
 466 of the fit regions depends heavily on the modeling of the jets. The other major sources of
 467 uncertainty come from background modelling and cross-section uncertainty. The pie charts in
 468 figure 32 show that for the modelling uncertainties that contribute most correspond to the most
 469 significant backgrounds.

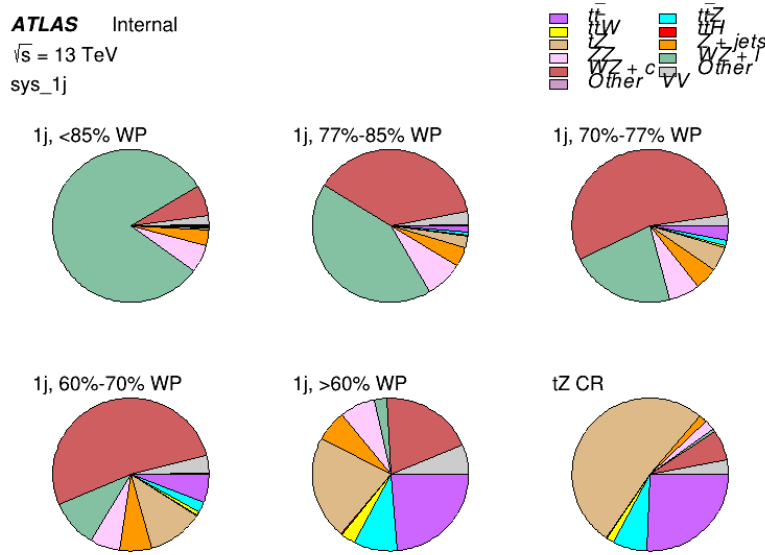


Figure 32: Post-fit background composition of the fit regions.

470 The correlations between these nuisance parameters are summarized in figure 33.

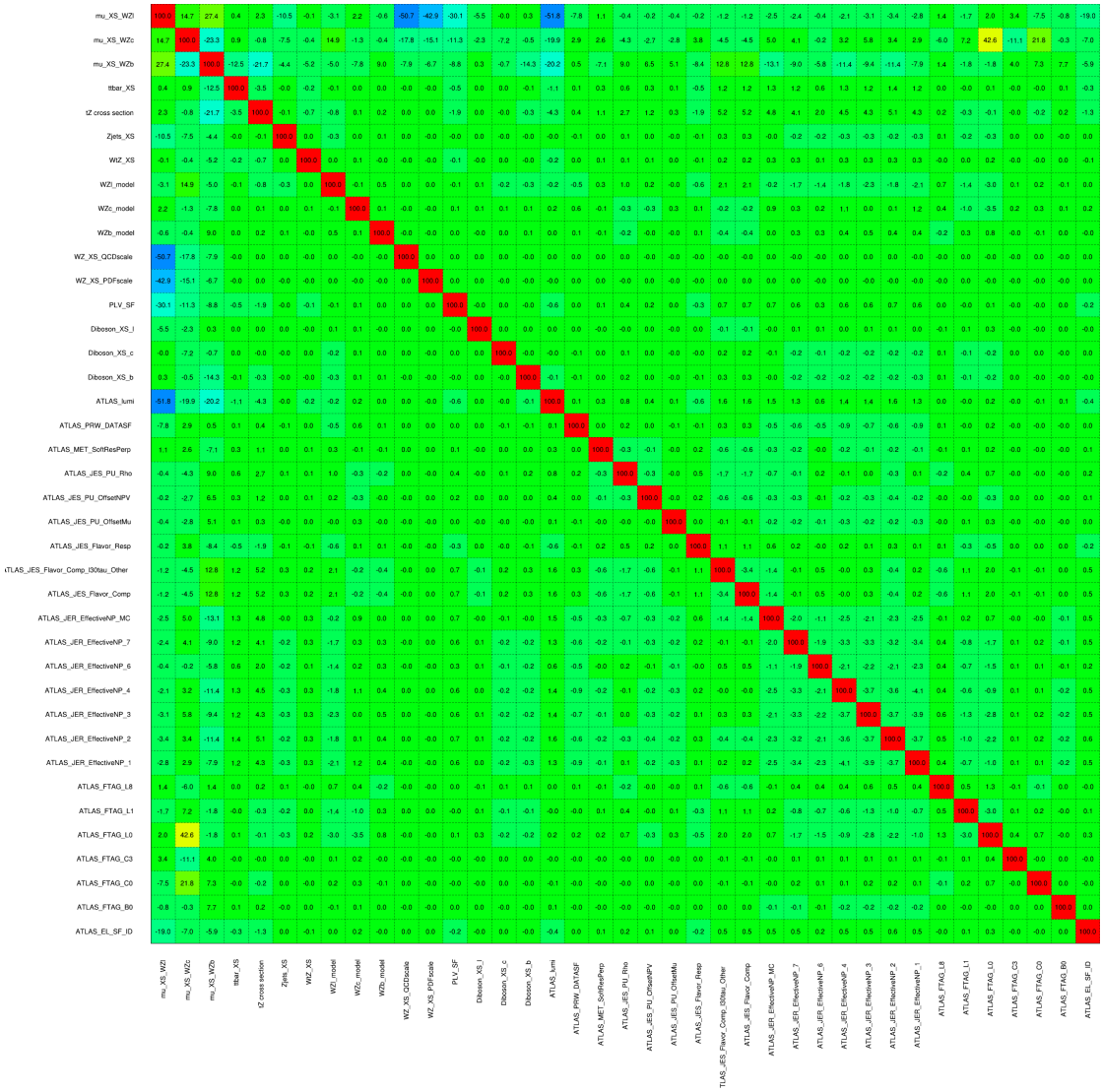


Figure 33: Correlations between nuisance parameters

471 The negative correlations between $\mu_{WZ+charm}$ and μ_{WZ+b} and $\mu_{WZ+light}$ are expected: WZ +
472 charm is present in both the WZ + b and WZ + light enriched regions, therefore increasing the
473 fraction of charm requires increasing the fraction of WZ + b and WZ + light. This reasoning
474 also explains the positive correlation between μ_{WZ+b} and $\mu_{WZ+light}$.

475 Two of the major backgrounds in the region with the highest purity of WZ + b are tZ and Other
476 VV + b, explaining the negative correlations between μ_{WZ+b} and the tZ cross section, and the
477 VV + b cross section.

⁴⁷⁸ The high correlation between the luminosity and $\mu_{WZ+light}$ arises from the fact that the uncer-
⁴⁷⁹ tainty on $\mu_{WZ+light}$ is very low (around 4%). Small changes in luminosity cause a change in
⁴⁸⁰ the yield of $WZ + light$ that is large compared to its uncertainty, producing a large correlation
⁴⁸¹ between these two parameters.

⁴⁸² 8.2 2-jet Fit Results

⁴⁸³ **The results of the fit are currently blinded.**

⁴⁸⁴ Pre-fit yields in each of the 2-jet fit regions are shown in figure [8.2](#).

	2j, <85% WP	2j, 77%-85% WP	2j, 70%-77% WP	2j, 60%-70% WP	2j, >60% WP	tZ CR 2j
WZ + b	13 ± 2	6.7 ± 0.5	5.6 ± 0.4	8.0 ± 0.6	31 ± 2	14 ± 1
WZ + c	260 ± 20	77 ± 6	41 ± 3	27 ± 3	11 ± 2	4.8 ± 0.6
WZ + l	1860 ± 150	90 ± 14	18 ± 3	5.8 ± 1.4	1.4 ± 0.4	0.25 ± 0.15
Other VV	7.63 ± 0.63	0.6 ± 0.5	0.16 ± 0.03	0.01 ± 0.01	0.1 ± 0.1	0.1 ± 0.1
ZZ	135 ± 20	14.1 ± 3.2	4.7 ± 0.8	4.0 ± 0.6	4.1 ± 0.7	3.1 ± 0.5
t <bar>t>W</bar>	0.8 ± 0.2	0.4 ± 0.1	0.5 ± 0.1	0.7 ± 0.2	4.3 ± 0.6	3.9 ± 0.6
t <bar>t>Z</bar>	14.7 ± 2.2	5.6 ± 0.8	4.5 ± 0.7	6.5 ± 1.1	25.4 ± 4.0	21.9 ± 3.4
rare Top	0.14 ± 0.04	0.07 ± 0.03	0.03 ± 0.02	0.09 ± 0.03	0.37 ± 0.07	0.6 ± 0.1
t <bar>t>WW</bar>	0.04 ± 0.03	0.02 ± 0.02	0.01 ± 0.01	0.01 ± 0.00	0.03 ± 0.03	0.01 ± 0.01
Z + jets	110.0 ± 22.9	9.6 ± 2.0	2.1 ± 0.50	1.6 ± 0.4	5.1 ± 1.1	1.5 ± 0.3
W + jets	0.0 ± 0.0	0.0 ± 0.0	0.0 ± 0.0	0.0 ± 0.0	0.0 ± 0.0	0.0 ± 0.0
V + γ	25 ± 18	0.5 ± 0.2	0.1 ± 0.1	0.1 ± 0.1	0.0 ± 0.02	0.05 ± 0.07
tZ	15.9 ± 2.9	6.9 ± 1.3	5.1 ± 1.0	8.0 ± 1.5	18.7 ± 3.2	36.4 ± 6.1
tW	0.9 ± 0.7	0.2 ± 0.3	0.0 ± 0.1	0.0 ± 0.0	0.8 ± 0.6	0.2 ± 0.2
WtZ	4.9 ± 2.5	1.5 ± 0.8	1.1 ± 0.6	1.3 ± 0.7	4.6 ± 2.4	3.3 ± 1.7
VVV	7.4 ± 0.3	1.0 ± 0.1	0.4 ± 0.1	0.2 ± 0.1	0.13 ± 0.03	0.04 ± 0.01
VH	19.5 ± 4.2	2.8 ± 1.6	0.7 ± 0.7	0.1 ± 0.2	0.0 ± 0.0	0.0 ± 0.0
t <bar>t></bar>	0.7 ± 0.4	0.1 ± 0.1	0.05 ± 0.06	0.15 ± 0.13	0.8 ± 0.5	2.3 ± 1.2
t <bar>t></bar>	6.8 ± 1.0	2.4 ± 0.5	1.8 ± 0.4	3.3 ± 0.6	8.4 ± 1.2	13.6 ± 1.7
t <bar>t>H</bar>	0.4 ± 0.1	0.2 ± 0.1	0.16 ± 0.02	0.23 ± 0.03	0.94 ± 0.11	1.03 ± 0.12
Total	2580 ± 160	229 ± 24	89 ± 13	69 ± 11	120 ± 15	108 ± 11

Table 16: Pre-fit yields in each of the 2-jet fit regions.

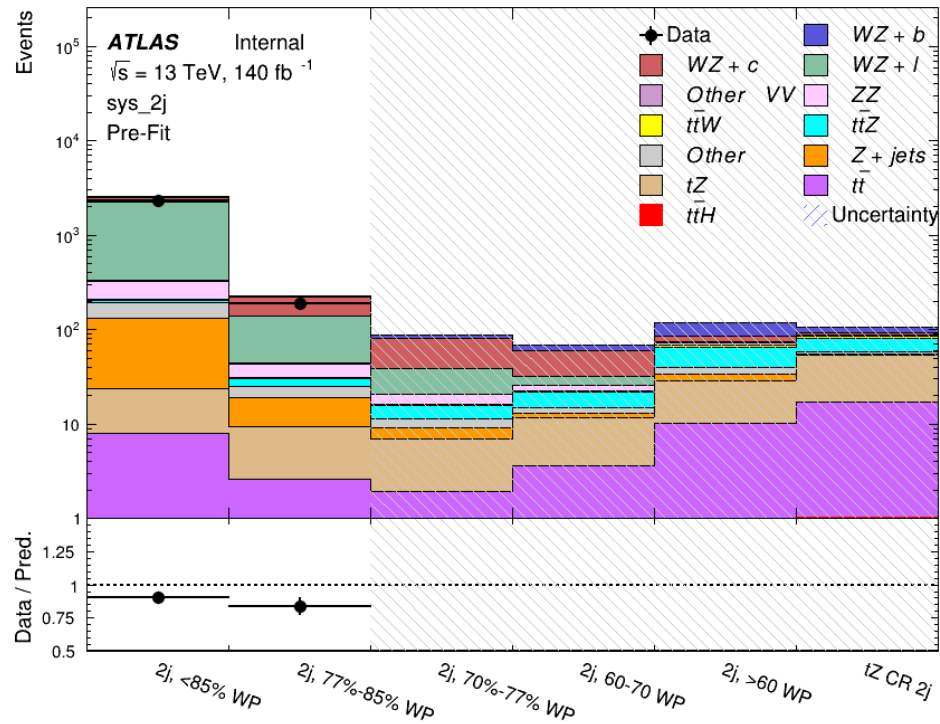


Figure 34: Pre-fit summary of the 2-jet fit regions.

485 The post-fit yields in each region are summarized in figure 8.2.

	2j, <85% WP	2j, 77%-85% WP	2j, 70%-77% WP	2j, 60%-70% WP	2j, >60% WP	tZ CR 2j
WZ + b	13 ± 6	6.7 ± 2.9	5.8 ± 2.5	8.0 ± 3.5	31 ± 13	14 ± 5
WZ + c	260 ± 60	77 ± 15	41 ± 8	26 ± 5	10.9 ± 2.4	4.8 ± 1.1
WZ + l	1860 ± 90	90 ± 12	17.6 ± 2.8	5.8 ± 1.3	1.4 ± 0.4	0.3 ± 0.2
Other VV	7.6 ± 0.6	0.3 ± 0.3	0.3 ± 0.1	0.1 ± 0.06	0.03 ± 0.02	0.1 ± 0.1
ZZ	145 ± 30	11.3 ± 4.4	2.7 ± 1.6	1.0 ± 0.3	4.0 ± 0.1	2.4 ± 0.1
t̄tW	0.8 ± 0.2	0.4 ± 0.1	0.54 ± 0.12	0.74 ± 0.15	4.3 ± 0.6	3.9 ± 0.6
t̄tZ	14.7 ± 2.2	5.6 ± 0.8	4.5 ± 0.7	6.5 ± 1.0	25.4 ± 3.9	21.9 ± 3.3
rare Top	0.14 ± 0.04	0.07 ± 0.03	0.03 ± 0.02	0.09 ± 0.03	0.4 ± 0.1	0.6 ± 0.1
t̄tWW	0.04 ± 0.03	0.02 ± 0.02	0.01 ± 0.01	0.01 ± 0.01	0.03 ± 0.03	0.01 ± 0.01
Z + jets	110 ± 23	9.6 ± 2.0	2.1 ± 0.5	1.6 ± 0.4	5.1 ± 1.1	1.5 ± 0.3
W + jets	0.0 ± 0.0					
V + γ	25 ± 19	0.5 ± 0.2	0.1 ± 0.1	0.13 ± 0.14	0.0 ± 0.02	0.05 ± 0.07
tZ	15.9 ± 2.7	6.9 ± 1.2	5.1 ± 0.9	8.0 ± 1.4	18.7 ± 3.0	36 ± 6
tW	0.1 ± 0.7	0.2 ± 0.3	0.0 ± 0.1	0.0 ± 0.0	0.8 ± 0.6	0.2 ± 0.2
WtZ	4.9 ± 2.5	1.5 ± 0.8	1.1 ± 0.6	1.3 ± 0.7	4.6 ± 2.3	3.3 ± 1.7
VVV	7.4 ± 0.3	1.0 ± 0.1	0.36 ± 0.03	0.19 ± 0.03	0.13 ± 0.03	0.04 ± 0.01
VH	19 ± 4	2.8 ± 1.6	0.7 ± 0.7	0.1 ± 0.2	0.0 ± 0.0	0.0 ± 0.0
t̄t	6.8 ± 1.0	2.4 ± 0.5	1.8 ± 0.4	3.3 ± 0.6	8.4 ± 1.2	13.6 ± 1.7
t̄tH	0.40 ± 0.05	0.19 ± 0.03	0.16 ± 0.02	0.23 ± 0.03	0.94 ± 0.11	1.03 ± 0.11
Total	2580 ± 60	229 ± 11	89 ± 6	69.1 ± 4.1	120 ± 10	108 ± 6

Table 17: Post-fit yields in each of the 2-jet fit regions.

⁴⁸⁶ A post-fit summary of the fitted regions is shown in figure 35:

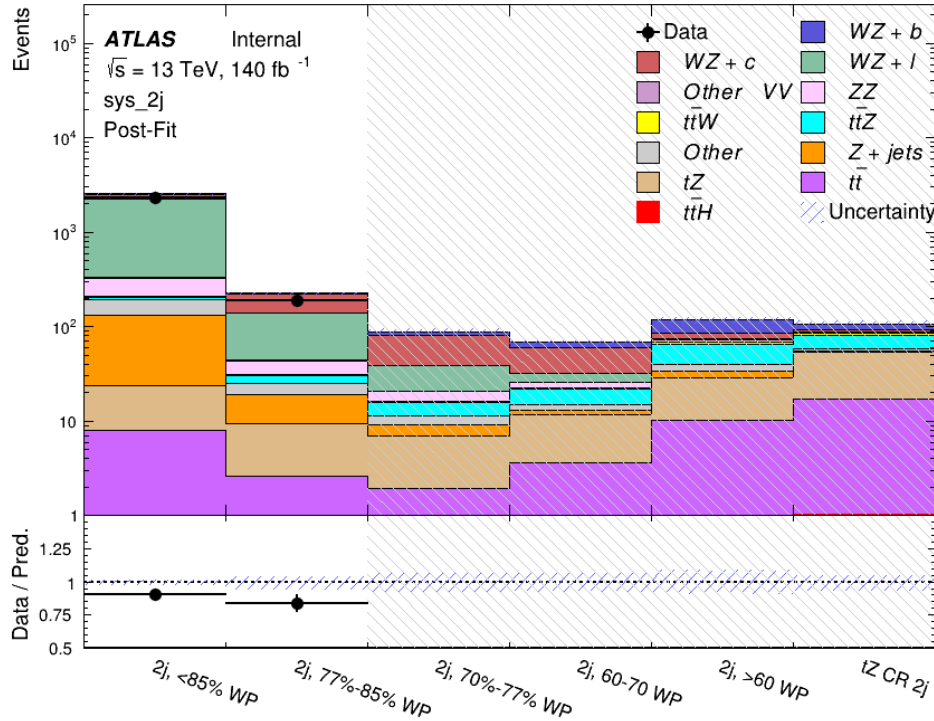


Figure 35: Post-fit summary of the fit over 2-jet regions.

487 The same set of systematic uncertainties consider for the 1-jet fit are included in the 2-jet fit as
 488 well. The impact of the most significant systematic uncertainties is summarized in table 18.

Uncertainty Source	$\Delta\mu$	
WZ + c cross-section	-0.1	0.14
Luminosity	-0.11	0.12
tZ cross-section	-0.11	0.11
Jet Energy Scale	-0.11	0.11
ttZ cross-section - QCD scale	-0.08	0.09
WZ + l cross-section	0.08	-0.07
WtZ cross-section	-0.07	0.07
Flavor tagging	0.05	0.05
Other VV + b cross-section	-0.05	0.05
Jet Energy Resolution	-0.04	0.04
Total	0.29	0.31

Table 18: Summary of the most significant sources of systematic uncertainty on the measurement of WZ + b 2-jet events.

⁴⁸⁹ The ranking and impact of those nuisance parameters with the largest contribution to the overall
⁴⁹⁰ uncertainty is shown in figure 36.

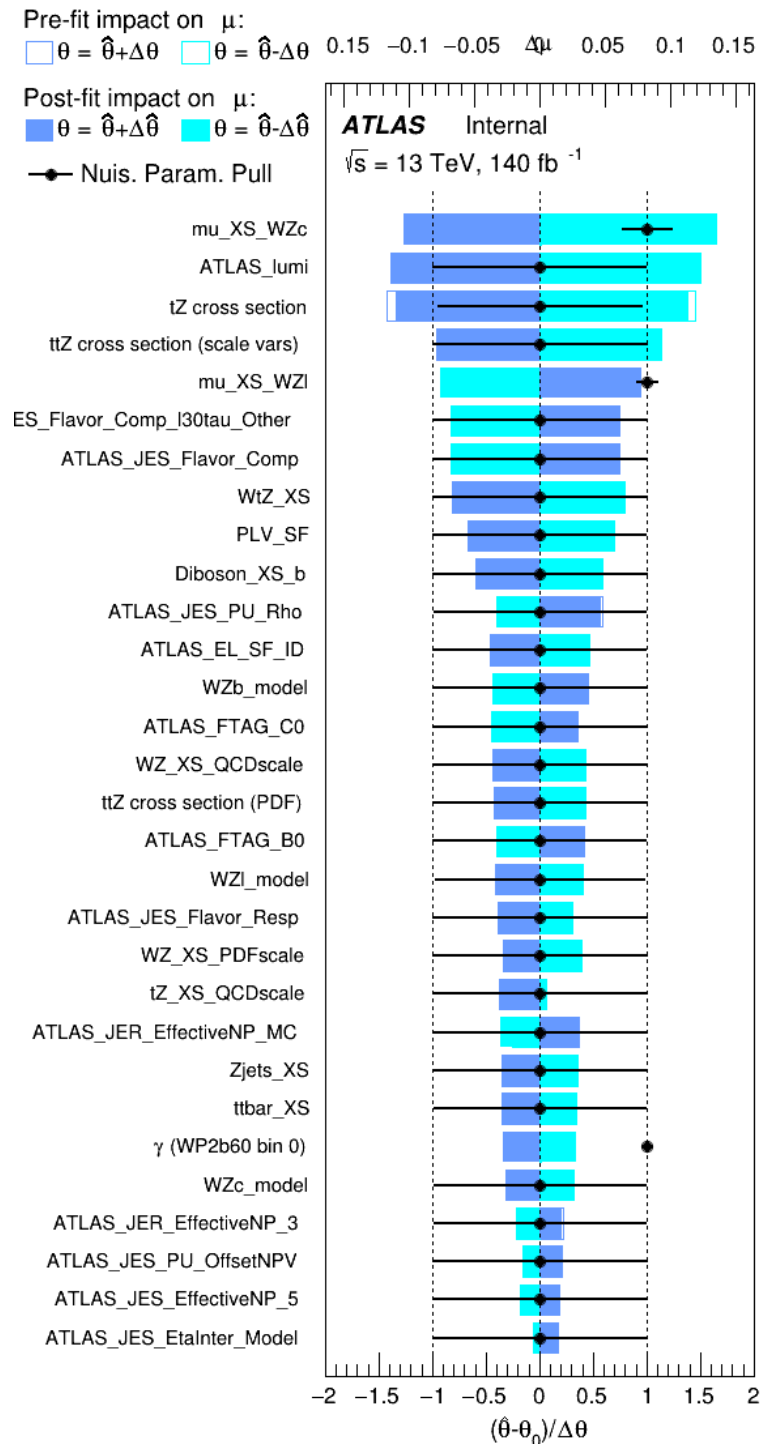


Figure 36: Impact of systematic uncertainties on the signal-strength of $WZ + b$ in 2-jet events.

491 The large impact of the Jet Energy Scale and Jet Flavor Tagging is unsurprising, as the shape
 492 of the fit regions depends heavily on the modeling of the jets. The other major sources of
 493 uncertainty come from background modelling and cross-section uncertainty. The pie charts in
 494 figure 37 show that for the modelling uncertainties that contribute most correspond to the most
 495 significant backgrounds.

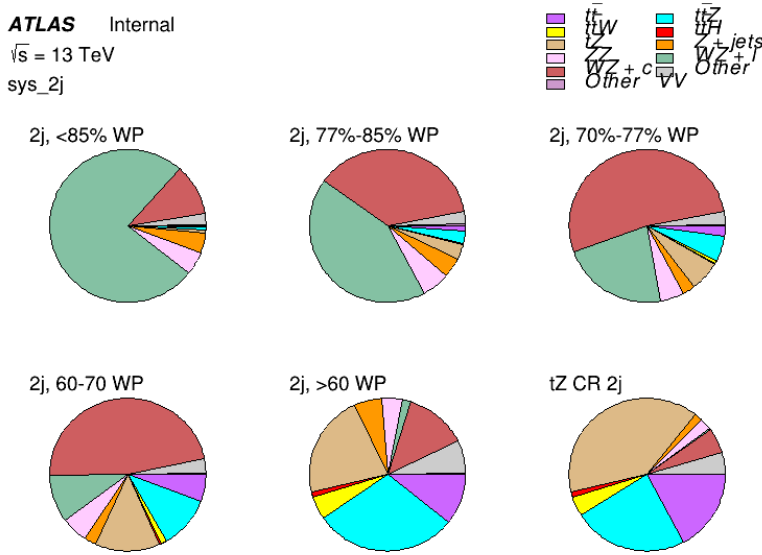


Figure 37: Post-fit background composition of the 2-jet fit regions.

496 The correlations between these nuisance parameters are summarized in figure 38.

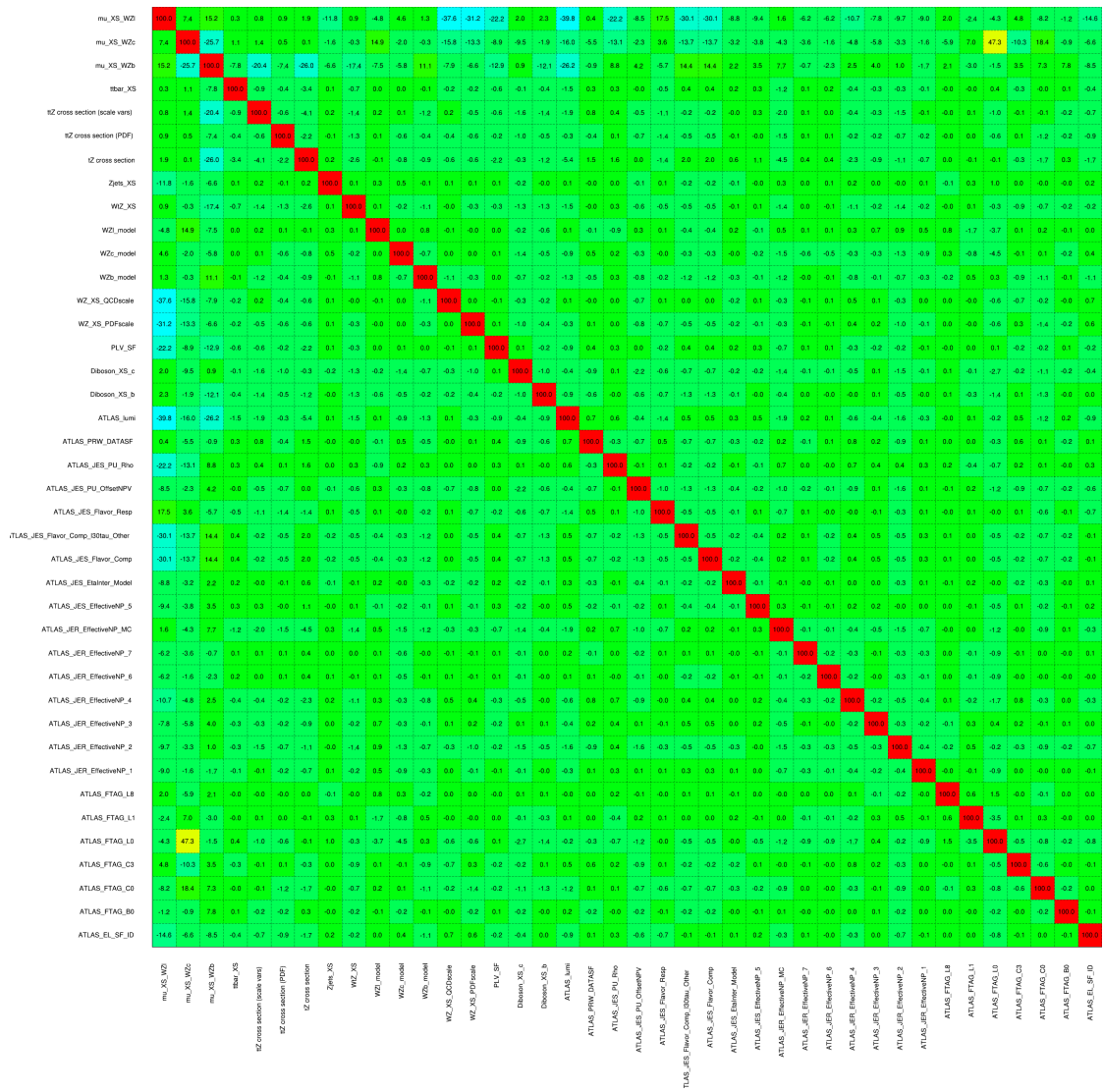


Figure 38: Correlations between nuisance parameters in the 2-jet fit

497 As in the 1-jet case, no significant, unexpected correlations are found between nuisance para-
 498 meters.

9 Conclusion

500 A measurement of $WZ + \text{heavy flavor}$ is performed using 140 fb^{-1} of $\sqrt{s} = 13 \text{ TeV}$ proton-
 501 proton collision data collected by the ATLAS detector at the LHC. This section will be include

502 **final results once unblinded.**

503 **Appendices**

504 **tZ Interference Studies**

505 Because it includes an on-shell Z boson as well as a b-jet and W from the top decay, tZ
506 production represents an identical final state to WZ + b-jet. This implies the possibility of matrix
507 level interference between these two processes not accounted for in the Monte Carlo simulations,
508 which consider the two processes independently. Truth level studies are performed in order to
509 estimate the impact of these interference effects.

510 In order to estimate the matrix level interference effects between tZ and WZ + b-jet, two different
511 sets of simulations are produced using MadGraph 5 [**Madgraph**] - one which simulates these
512 two processes independently, and another where they are produced simultaneously, such that
513 interference effects are present. These two sets of samples are then compared, and the difference
514 between them can be taken to represent any interference effects.

515 MadGraph simulations of 10,000 tZ and 10,000 WZ + b-jet events are produced, along with
516 20,000 events where both are present, in the fiducial region where three leptons and at least one
517 jet are produced.

518 A selection mimicking the preselection used in the main analysis is applied to the samples: The
519 SS leptons are required to have $p_T > 20$ GeV, and > 10 GeV is required for the OS lepton. The
520 associated b-jet is required to have $p_T > 25$ GeV, and all physics objects are required to fall in a
521 range of $|\eta| < 2.5$.

522 The kinematics of these samples after the selection has been applied are shown below:

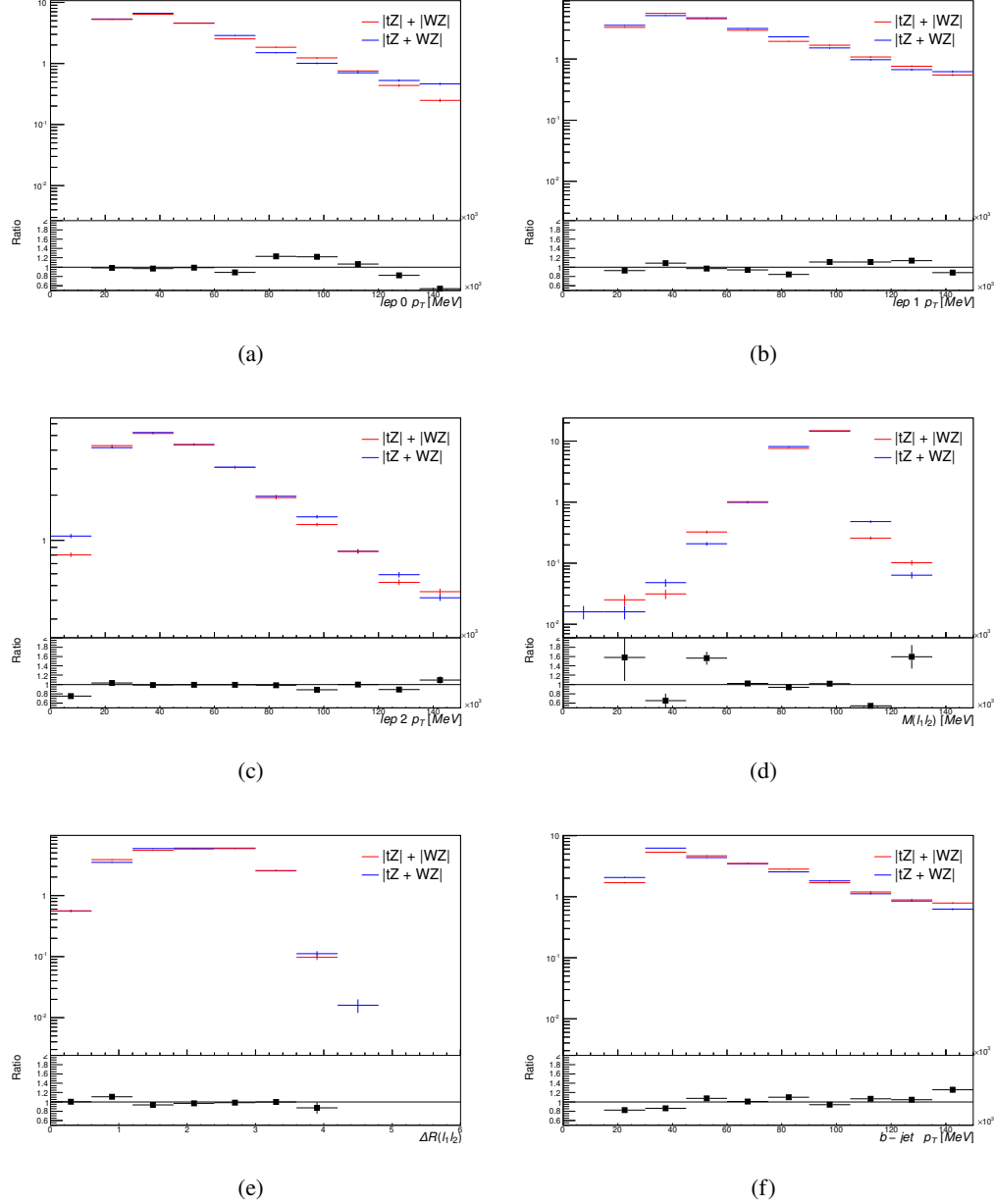


Figure 39: Comparisons between (a) the p_T of the lepton from the W, (b) and (c) show the p_T of the lepton from the Z, (d) the invariant mass of the Z-candidate, (e) ΔR of the leptons from the Z, and (f) the p_T of the b-jet, for WZ and tZ events generated with interference effects (blue) and without interference effects (red).

523 The overall cross-section of the two methods agree within error, and no significant differences
 524 in the kinematic distributions are seen. It is therefore concluded that interference effects do not

525 significantly impact the results.

526 **Alternate tZ Inclusive Fit**

527 While tZ is often considered as a distinct process from WZ + b, this could also be considered part
 528 of the signal. Alternate studies are performed where, using the same framework as the nominal
 529 analysis, a measurement of WZ + b is performed that includes tZ as part of WZ+b.

530 Because of this change, the tZ CR is no longer necessary, and only the five pseudo-continuous
 531 b-tag regions are used in the fit. Further, systematics related to the tZ cross-section are removed
 532 from the fit, as they are now encompassed by the normalization measurement of WZ + b. All
 533 other systematic uncertainties are carried over from the nominal analysis.

534 A post-fit summary of the 1-jet regions used in the fit are shown in figure 40.

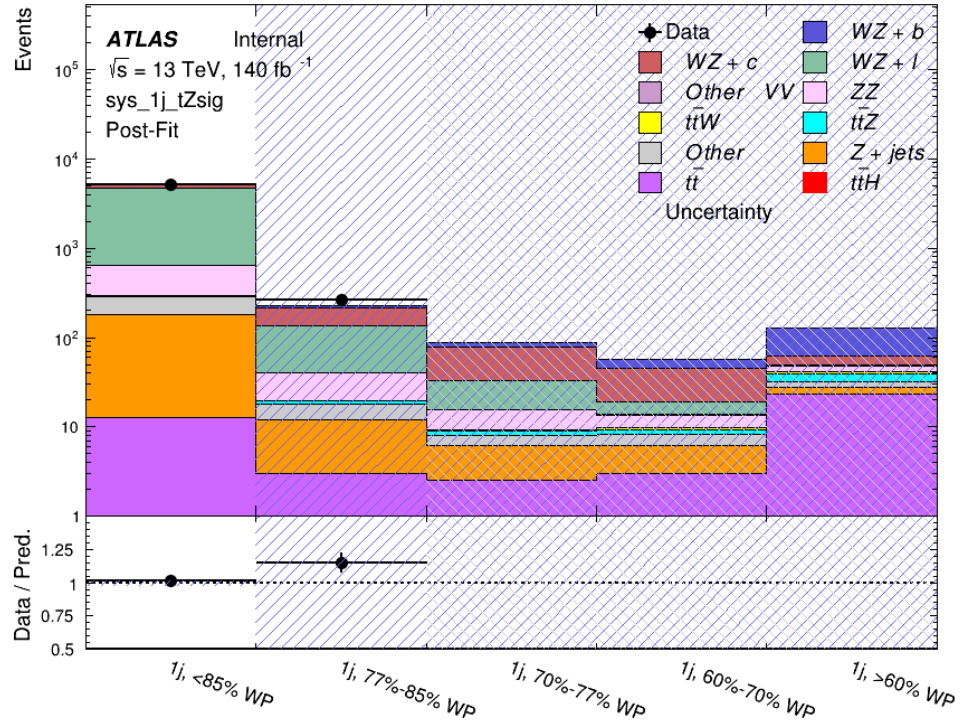


Figure 40: Post-fit summary of the 1-jet fit regions.

535 An expected WZ + b cross-section of $4.1^{+0.78}_{-0.74}(\text{stat})^{+0.53}_{-0.52}(\text{sys}) \text{ fb}$ is extracted from the fit, with
 536 an expected significance of 4.0σ .

537 The impact of the predominate systematics are summarized in table 19.

Uncertainty Source	$\Delta\mu$	
WZ + light cross-section	0.08	-0.08
Jet Energy Scale	-0.06	0.08
Luminosity	-0.05	0.06
WZ + charm cross-section	-0.04	0.05
Other Diboson + b cross-section	-0.04	0.04
WZ cross-section - QCD scale	-0.04	0.03
t <bar>t</bar>	-0.03	0.03
Jet Energy Resolution	-0.03	0.03
Flavor tagging	-0.03	0.03
Z+jets cross section	-0.02	0.02
Total Systematic Uncertainty	-0.15	0.16

Table 19: Summary of the most significant sources of systematic uncertainty on the measurement of WZ + b with exactly one associated jet.

538 A post-fit summary of the 2-jet regions used in the fit are shown in figure 41.

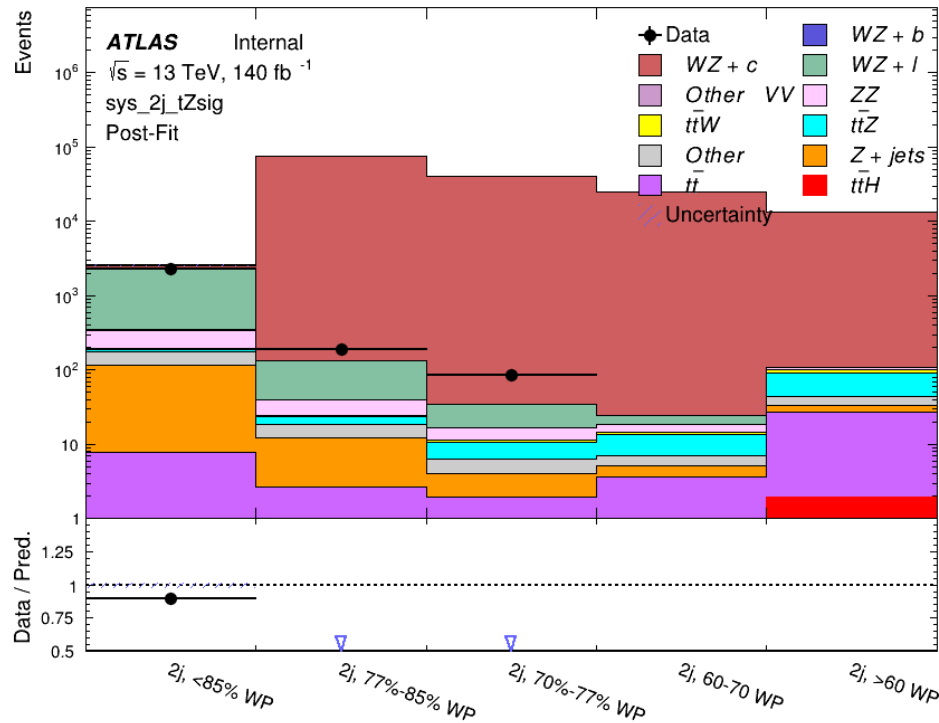


Figure 41: Post-fit summary of the 1-jet fit regions.

539 An expected WZ + b cross-section of $5.9^{+0.9}_{-0.9}(\text{stat})^{+0.9}_{-0.8}(\text{sys}) \text{ fb}$ is extracted from the fit, with an
 540 expected significance of 5.3σ .

541 The impact of the predominate systematics are summarized in table 20.

Uncertainty Source	$\Delta\mu$	
Luminosity	-0.07	0.07
Jet Energy Scale	0.06	0.05
ttZ cross-section - QCD scale	-0.05	0.05
WZ+l cross-section	0.05	-0.05
WZ+c cross-section	-0.03	0.05
WtZ cross-section	-0.03	0.03
WZ cross-section QCDscale	-0.03	0.03
Diboson cross-section b	-0.03	0.03
WZ cross-section - PDF	-0.03	0.03
Flavor Tagging	0.03	0.02
Total Systematic Uncertainty	-0.14	0.16

Table 20: Summary of the most significant sources of systematic uncertainty on the measurement of WZ + b with exactly one associated jet.

542 References

- 543 [1] M. Aaboud et al. ‘Observation of electroweak $W^\pm Z$ boson pair production in association
 544 with two jets in pp collisions at $\sqrt{s} = 13$ TeV with the ATLAS detector’. In: *Phys.*
 545 *Lett.* B793 (2019), pp. 469–492. doi: [10.1016/j.physletb.2019.05.012](https://doi.org/10.1016/j.physletb.2019.05.012). arXiv:
 546 [1812.09740 \[hep-ex\]](https://arxiv.org/abs/1812.09740).
- 547 [2] T. Gleisberg et al. ‘Event generation with SHERPA 1.1’. In: *JHEP* 02 (2009), p. 007. doi:
 548 [10.1088/1126-6708/2009/02/007](https://doi.org/10.1088/1126-6708/2009/02/007). arXiv: [0811.4622 \[hep-ph\]](https://arxiv.org/abs/0811.4622).
- 549 [3] ATLAS Collaboration. *Electron efficiency measurements with the ATLAS detector using*
 550 *the 2015 LHC proton–proton collision data*. ATLAS-CONF-2016-024. 2016. URL: <https://cds.cern.ch/record/2157687>.
- 551 [4] ATLAS Collaboration. ‘Measurement of the muon reconstruction performance of the
 552 ATLAS detector using 2011 and 2012 LHC proton–proton collision data’. In: *Eur. Phys.*
 553 *J. C* 74 (2014), p. 3130. doi: [10.1140/epjc/s10052-014-3130-x](https://doi.org/10.1140/epjc/s10052-014-3130-x). arXiv: [1407.3935](https://arxiv.org/abs/1407.3935)
 555 [hep-ex].
- 556 [5] *Evidence for the associated production of the Higgs boson and a top quark pair with the*
 557 *ATLAS detector*. Tech. rep. ATLAS-CONF-2017-077. Geneva: CERN, Nov. 2017. URL:
 558 <https://cds.cern.ch/record/2291405>.
- 559 [6] ATLAS Collaboration. *Jet Calibration and Systematic Uncertainties for Jets Reconstructed*
 560 *in the ATLAS Detector at $\sqrt{s} = 13$ TeV*. ATL-PHYS-PUB-2015-015. 2015. URL:
 561 <https://cds.cern.ch/record/2037613>.
- 562 [7] ATLAS Collaboration. *Selection of jets produced in 13 TeV proton–proton collisions with*
 563 *the ATLAS detector*. ATLAS-CONF-2015-029. 2015. URL: <https://cds.cern.ch/record/2037702>.
- 564 [8] ATLAS Collaboration. ‘Performance of pile-up mitigation techniques for jets in pp col-
 565 lisions at $\sqrt{s} = 8$ TeV using the ATLAS detector’. In: *Eur. Phys. J. C* 76 (2016), p. 581.
 566 doi: [10.1140/epjc/s10052-016-4395-z](https://doi.org/10.1140/epjc/s10052-016-4395-z). arXiv: [1510.03823 \[hep-ex\]](https://arxiv.org/abs/1510.03823).
- 567 [9] ATLAS Collaboration. *Performance of missing transverse momentum reconstruction with*
 568 *the ATLAS detector in the first proton–proton collisions at $\sqrt{s} = 13$ TeV*. ATL-PHYS-
 569 PUB-2015-027. 2015. URL: <https://cds.cern.ch/record/2037904>.
- 570 [10] P. S. A. Hoecker. ‘TMVA 4 Toolkit for Multivariate Data Analysis with ROOT’. In:
 571 *arXiv:physics/0703039* (2013).
- 572 [11] F. Cardillo et al. ‘Measurement of the fiducial and differential cross-section of a top quark
 573 pair in association with a Z boson at 13 TeV with the ATLAS detector’. In: ATL-COM-
 574 PHYS-2019-334 (Apr. 2019). URL: <https://cds.cern.ch/record/2672207>.
- 575 [12] ATLAS Collaboration. ‘Luminosity determination in pp collisions at $\sqrt{s} = 7$ TeV using
 576 the ATLAS detector at the LHC’. In: *Eur. Phys. J. C* 71 (2011), p. 1630. doi: [10.1140/epjc/s10052-011-1630-5](https://doi.org/10.1140/epjc/s10052-011-1630-5). arXiv: [1101.2185 \[hep-ex\]](https://arxiv.org/abs/1101.2185).

- 579 [13] G. Aad et al. ‘Jet energy resolution in proton-proton collisions at $\sqrt{s} = 7$ TeV recorded
580 in 2010 with the ATLAS detector’. In: *The European Physical Journal C* 73.3 (Mar.
581 2013), p. 2306. ISSN: 1434-6052. DOI: [10.1140/epjc/s10052-013-2306-0](https://doi.org/10.1140/epjc/s10052-013-2306-0). URL:
582 <https://doi.org/10.1140/epjc/s10052-013-2306-0>.
- 583 [14] A. Collaboration. ‘Performance of b -jet identification in the ATLAS experiment’. In:
584 *Journal of Instrumentation* 11.04 (2016), P04008. URL: <http://stacks.iop.org/1748-0221/11/i=04/a=P04008>.
585